

Title	Regulated phase separation in nanopatterned protein-polysaccharide thin films by spin coating
Authors	Banta, Russell A.;Collins, Timothy W.;Curley, Ricky;O'Connell, John;Young, Paul W.;Holmes, Justin D.;Flynn, Eoin J.
Publication date	2020-03-18
Original Citation	Banta, R. A., Collins, T. W., Curley, R., O'Connell, J., Young, P. W., Holmes, J. D. and Flynn, E. J. (2020) 'Regulated phase separation in nanopatterned protein-polysaccharide thin films by spin coating', Colloids and Surfaces B-Biointerfaces, 190, 110967 (11 pp). doi: 10.1016/j.colsurfb.2020.110967
Type of publication	Article (peer-reviewed)
Link to publisher's version	https://www.sciencedirect.com/science/article/pii/S0927776520301971 - 10.1016/j.colsurfb.2020.110967
Rights	© 2020 Elsevier B. V. All rights reserved. This manuscript version is made available under the CC BY-NC-ND 4.0 license. - https://creativecommons.org/licenses/by-nc-nd/4.0/
Download date	2024-10-04 22:22:00
Item downloaded from	https://hdl.handle.net/10468/9835

1 **Regulated Phase Separation in**
2 **Nanopatterned Protein-Polysaccharide Thin Films by Spin Coating**

3
4 Russell A. Banta^{a,b,c}, Timothy W. Collins^{a,b,c}, Ricky Curley^{a,b,c}, John O'Connell^{a,b,c},
5 Paul W. Young^{b, d}, Justin D. Holmes^{a,b,c} and Eoin J. Flynn^{a,b,c*}

6
7 ^aSchool of Chemistry, University College Cork, Cork, Ireland.

8 ^bEnvironmental Research Institute, Lee Road, University College Cork, Cork, Ireland.

9 ^cAMBER@CRANN, Trinity College Dublin, Dublin 2, Ireland.

10 ^dSchool of Biochemistry and Cell Biology, University College Cork, Ireland.

11
12 *To whom correspondence should be addressed: Tel: +35-321-490-1961; E-mail:
13 eoin.flynn@ucc.ie

14
15 **Keywords:** protein, polysaccharide, biopolymer, patterning, morphology, phase separation,
16 Ostwald ripening.

17
18 **Abstract**

19 Patterned films are essential to the commonplace technologies of modern life. However, they
20 come at high cost to the planet, being produced from non-renewable, petrochemical-derived
21 polymers and utilising substrates that require harsh, top-down etching techniques.
22 Biopolymers offer a cheap, sustainable and viable alternative easily integrated into existing
23 production techniques. We describe a simple method for the production of patterned
24 biopolymer surfaces and the assignment of each biopolymer domain, which allows for selective

25 metal incorporation used in many patterning applications. Protein and polysaccharide domains
26 were identified by selective etching and metal incorporation; a first for biopolymer blends.
27 Morphologies akin to those observed with synthetic polymer blends and block-copolymers
28 were realised across a large range of feature diameter (200 nm to - 20 μm) and types (salami
29 structure, continuous, porous and droplet-matrix). The morphologies of the films were
30 tuneable with simple recipe changes, highlighting that these biopolymer blends are a feasible
31 alternative to traditional polymers when patterning surfaces. The protein to polysaccharide
32 ratio, viscosity, casting method and spin speed were found to influence the final film
33 morphology. High protein concentrations generally resulted in porous structures whereas
34 higher polysaccharide concentrations resulted in spherical discontinuous domains. Low spin
35 speed conditions resulted in growth of protuberances ranging from 200 nm to 22 μm in
36 diameter, while higher spin speeds resulted in more monodisperse features, with smaller
37 maximal diameter structures ranging from 300 nm to 12.5 μm .

38

39 **Introduction**

40 There is an urgent and growing need for micro- and nano-structured surfaces that can be
41 produced at low environmental and economic cost. Micro- and nano-structured surfaces are
42 essential to an array of advanced and emerging technologies. In 2016 the OECD identified 40
43 key emerging technologies for the future, including the “internet of things” smart devices, light
44 technologies, regenerative medicine and tissue engineering, nanomaterials, nanodevices,
45 carbon nanotubes, functional materials, synthetic biology, and marine and tidal power
46 technologies. One fifth of these require patterned thin-films as integral components or as
47 essential aspects of their production processes [1].

48

49 Micro- and nano-structured surfaces occur throughout the natural world and exhibit a
50 range of useful properties; self-cleaning and hydrophobicity (lotus leaf)[2]; anti-reflectivity
51 (moth eyes)[3]; iridescence (butterfly wings)[3]; anti-ice formation (kale) [4]; and anti-fouling
52 (shark skin)[5], to name only a few. Current human manufacturing of equivalent surfaces uses
53 top-down and bottom-up approaches: top-down is expensive, wasteful, not readily scalable,
54 and generally restricted to planar surfaces.[3] Bottom-up requires the use of block co-polymers
55 (BCPs) which can be expensive, are synthetically derived, require environmentally damaging
56 organic solvents and require intricate control of the polymer-surface interface via brush
57 layers.[6] Feature diameter and spacing is limited to sub-100 nm due to the kinetic penalties
58 imposed on high molecular weight BCPs requiring long annealing times, limiting their
59 applications in the optics industry. Additionally, refining BCPs of a high molecular weight to
60 obtain a polydispersity index (PDI) close to 1 is difficult and costly.[3]

61 In contrast, to BCPs and other synthetic polymers, proteins innately have a PDI of 1, are
62 cheap, abundant, renewable, do not require the use of toxic solvents and are easy to
63 manufacture.[7] More generally, biopolymers (proteins and polysaccharides) are well-defined
64 with varied functionality[8], hydrophilic, photostable, nontoxic, biocompatible[9], [10] and
65 have predictable viscosities.[11] The domain sizes of features in polymer blends (synthetic
66 and biopolymer) have been shown to exceed to 10 μm , although feature size showed
67 considerable variance.[12]–[19] For decades biopolymer blends have been utilised in food
68 texturing[15], [16], [19], [20], with few notable examples using biopolymer blends beyond
69 this.[21], [22], [31], [32], [23]–[30] These, however, incorporated synthetic polymer additives,
70 biopolymer derivatives, and/or specialist enzymes for etching or functionalisation of patterned
71 surfaces. This renders these techniques either unsuitable for large scale manufacturing or
72 environmentally damaging. Protein blends are expected to become prevalent in electronic,
73 optical, chemical, mechanical, biomedical and nanotech applications in the coming years.[33]

74 However, the use of biopolymer blend thin films in materials science for surface patterning is
75 further limited by the relative infancy of the field.[31]

76 The aim of this study was the further development of bovine serum albumin (BSA) and
77 chitosan (Ch) blend thin films, using a protic solvent (formic acid, FA) to promote segregative
78 phase separation in a rapid and facile manner. Current efforts to replace BCPs involve the use
79 of synthetic polymer blends to generate patterns. However, as with BCPs, these are not
80 renewable. To offer an alternative, renewable solution to both BCPs and synthetic polymer
81 blends, biopolymer blend thin films must show that they can achieve similar patterns, using
82 established methods. To this end, BSA and Ch were chosen as our biopolymers. BSA and Ch
83 may be blended without fear of gelation when subjected to shear forces.[34] Ch is also
84 antimicrobial[35], biocompatible and biodegradable, increasing the number of possible
85 applications.[36] Finally, both BSA[37] and Ch[38], [39] can selectively bind metals, similar
86 to BCPs. Synthetic polymer blends utilize selective removal of one polymer domain, followed
87 by deposition of a metal to generate a patterned hard mask. In our work, we successfully
88 removed the protein domain using a buffer solution, and selectively incorporated metal into the
89 polysaccharide domain. BSA-Ch blends achieve feature diameters comparable with synthetic
90 polymer blends.[3], [40], [41] This method could be easily employed in other studies of
91 biopolymer blends. Furthermore, this is the first time a hard mask has been produced with
92 bottom-up biopolymer blends. Lastly, we have successfully differentiated the growth
93 mechanisms occurring with dissimilar blend compositions.

94

95 **Experimental**

96 **Biopolymers, Casting Solutions and Substrate**

97 Low molecular weight chitosan (Ch, 50-190 kDa, > 75 % deacetylation) and bovine serum
98 albumin (BSA, lyophilised powder, \geq 96 %, molecular weight ~66 kDa) were purchased from
99 Sigma Aldrich. While the Ch we sourced was the deacetylated form of chitin (i.e. a chitin
100 derivative, which may be considered a semisynthetic), Ch may also be sourced from fungal
101 biomass without the need for derivatization.[42] Ch is renewable, and it is much more easily
102 solubilized than chitin. Hence it was chosen for this work. Low molecular weight chitosan
103 was chosen as it was shown previously shown to be easily solubilized in the FA, while not
104 being excessively viscous.[34] Substrates used in all cases were Fisherbrand™ Microscopic
105 Slides with Ground Edges (plain) or planar substrates. Highly polished single-crystal silicon
106 <100> wafers (p-type, boron) with a native oxide layer of ~2 nm were also used. For FTIR,
107 XPS, water contact angle, and selective metal inclusion, samples were deposited on a Si
108 substrate. This was done to prevent any deformation of a glass substrate during annealing. The
109 solvent used was formic acid (FA), 98+ %, pure (ACROS Organics™) and was diluted to 90
110 % w/v with distilled water before use. Casting solutions were prepared using 90 % formic acid
111 as the solvent to ensure that the biopolymers were below their isoelectric point in solution and
112 so, positively charged.

113

114 **Solution Preparation**

115 Biopolymers blend preparation may be found in our previous work, or in our Supporting
116 Information. In short, stock solutions were made by dissolving biopolymers in 90 % FA, and
117 stored at -20 °C. Before coating, stock solutions mixed with one another and diluted with fresh
118 FA.[34] 5 solutions were prepared. 4 w/v% BSA 1 w/v% Ch (4:1 blend ratio), 2 w/v% BSA

119 1 w/v% Ch (2:1 blend ratio), 1 w/v% BSA 1 w/v% Ch (1:1 blend ratio), 1 w/v% BSA 2 w/v%
120 Ch (1:2 blend ratio) and 1 w/v% BSA 4 w/v% Ch (1:4 blend ratio).

121

122 **Coating Preparation**

123 *Thin-film Casting*

124 Thin-films were prepared using a spin coater (Speciality Coating Systems, 6800 Spin Coater
125 Series) to produce biopolymer solution coatings of uniform thickness. Standard conditions: 30
126 s spin time (ramp time 5 s, dwell 25 s). Substrates were glass slides onto which single
127 biopolymer solutions were cast. Temperature and humidity was maintained at approx. 18 °C
128 and 65 % relative humidity. Monitoring of humidity and ambient temperature was done by
129 *HOBO MX Temp/RH Logger* sensor.

130

131 *Atomic Force Microscopy (AFM)*

132 Sample morphology was analysed by atomic force microscopy (AFM) using a Park
133 Systems, XE-100 instrument under ambient conditions in non-contact mode, and this
134 methodology was used in our previous work.[34] Scans were performed in non-contact mode
135 with high resolution, silicon micro-cantilever tips. Topographic images were recorded at a
136 resonance frequency of 270-300 kHz. Images were analysed using *Park XEI* and *Gwyddion*,
137 and resulting data analysed using *Origin*. Images were flattened by removal of the background
138 plane (using a first or second regression order). Features were then identified using the
139 *Gwyddion* watershed algorithm for analysis, and descriptive statistics calculated using
140 "Microcal Origin" software. Surface roughness (nm) and surface area ratios (%) were
141 measured using "XEI" software. RMS (*root means square arithmetical mean roughness or*
142 *root means square average roughness*) is the average between the height deviations and the
143 mean line/surface, taken over the evaluation length/area. Surface area ratios (%) were

144 calculated by the following formula: Surface Area Ratio (%) = 100 (%) × (Geometric Area –
145 Surface Area) / (Geometric Area). Surface feature diameters were measured using the
146 Gwyddion watershed algorithm for scanning probe microscopy (approx. 1000 features). Film
147 thickness was determined by AFM. AFM height scans were performed on areas which had
148 been scratched to expose the underlying substrate.[26]

149

150 *X-Ray photoelectron spectroscopy (XPS)*

151 XPS spectra were acquired on an Oxford Applied Research Escabase XPS system equipped
152 with a CLASS VM 100 mm mean radius hemispherical electron energy analyser with a five-
153 channel detector arrangement in an analysis chamber with a base pressure of 10×10^{-10} mbar.
154 Survey scans were acquired between 0-1000 eV with a step size of 0.7 eV, a dwell time of 0.5
155 s and pass energy of 50 eV. Core level scans were acquired at the applicable binding energy
156 range for each core level, with a step size of 0.1 eV, dwell time of 0.1 s and pass energy of 20
157 eV averaged over 20 scans. A non-monochromated Al- $\kappa\alpha$ x-ray source at 200 W power was
158 used for all scans. Multiplier voltage was maintained at 2.0 kV for all acquisitions. All spectra
159 were acquired at a take-off angle of 90° with respect to the analyser axis and were charge
160 corrected with respect to the C 1s photoelectric line by rigidly shifting the binding energy scale
161 to 285 eV. Data were processed using CasaXPS software where a Shirley background
162 correction was applied and peaks were fitted to Voigt profiles.

163 *Attenuated Total Reflection Fourier Transform Infra-Red (ATR-FTIR) Spectroscopy*

164 Infrared spectra were recorded on a PerkinElmer Spectrum 2 FT-IR Spectrometer. Perkin-
165 Elmer Spectrum v5.0.1 software was used to perform baseline corrections and evaluate spectra.
166 Each spectrum was scanned between 400 and 4000 cm^{-1} with a resolution of 4 cm^{-1} and a
167 minimum of 64 scans were collected and averaged in order to gain good quality spectra.

168

169 *Selective Etching*

170 A wet etch was used in order to selectively remove BSA over Ch due to its limited solubility.

171 [43] Biopolymer blend films were crosslinked with a 20 wt% glutaraldehyde solution for 20

172 hr. Coated substrates were immersed in a buffered solution stirring for 20 hr at 300 rpm.

173 Buffered solutions contained 200 mM Tris-HCl, pH 8.8. The substrate was then washed

174 thoroughly with deionised water to remove residual salt. Finally, the substrate was washed

175 with isopropanol alcohol and dried under nitrogen for analysis.

176

177 *Selective metal inclusion*

178 To confirm the results of the selective etching of BSA using a basic buffer solution, and identify

179 the Ch domain, selective inclusion of the metal into the Ch domain used. As a 1:1 BSA-Ch

180 blend used to identify the BSA domain using a selective etch, the 1:1 BSA-Ch blend was also

181 used for selective metal inclusion. 1:1 blend films were prepared as described in the Thin-film

182 Casting section, producing a film with discontinuous spheres in a matrix. After casting, films

183 were crosslinked with a 20 wt% glutaraldehyde solution for 20 hr to prevent oversaturation of

184 metals in the Ch domain. 1 wt% FeCl₃ solutions were produced with anhydrous ethanol.

185 Biopolymer blend films were covered with 1 ml of metal solution for 15 s before spin coating.

186 The films were then immediately spin coated for 30 s (3000 rpm, ramp time 5 s, dwell 25 s).

187 The samples were then oxidised in a furnace at 550 °C for 2 hr. Calcination at 800 °C for 20

188 hr was used to remove the biopolymer template and any residual organic residue. No other

189 processing steps were needed.

190

191 *Water Contact Angle*

192 Water contact angle measurements were obtained using the Ossila Contact Angle Goniometer
193 (error $\pm 1^\circ$) and accompanying software Ossila Contact Angle v1.0. A deionised water droplet
194 (5 μL) was delivered to the coated surface by a calibrated variable pipettor. Contact angles
195 were measured in triplicate as a function of time. Measurements were taken at 10 s intervals
196 over 160 s including measurements at 0 and 160 s.

197

198 **Results and Discussion**

199 **Single Polymer Solution Thin-Films**

200 AFM images (see **Figure S1** in Supporting Information) showed that thin-films cast from the
201 two individual biopolymers (Ch and BSA) did not produce any phase separated patterns. Neat
202 BSA films were totally featureless (**Figure S1**), while Ch showed partially aggregated
203 structures, likely due to its limited solubility. Glass slides were smooth and featureless. This
204 shows that features present in subsequent composite biopolymer films are due solely to the
205 composite formation mechanisms and not due to structures from an individual biopolymer.
206 This is consistent with our previous findings.[34]

207

208 **BSA-Ch Thin-Films**

209 *Thin-films from Phase Separation of BSA-Ch-FA Solutions*

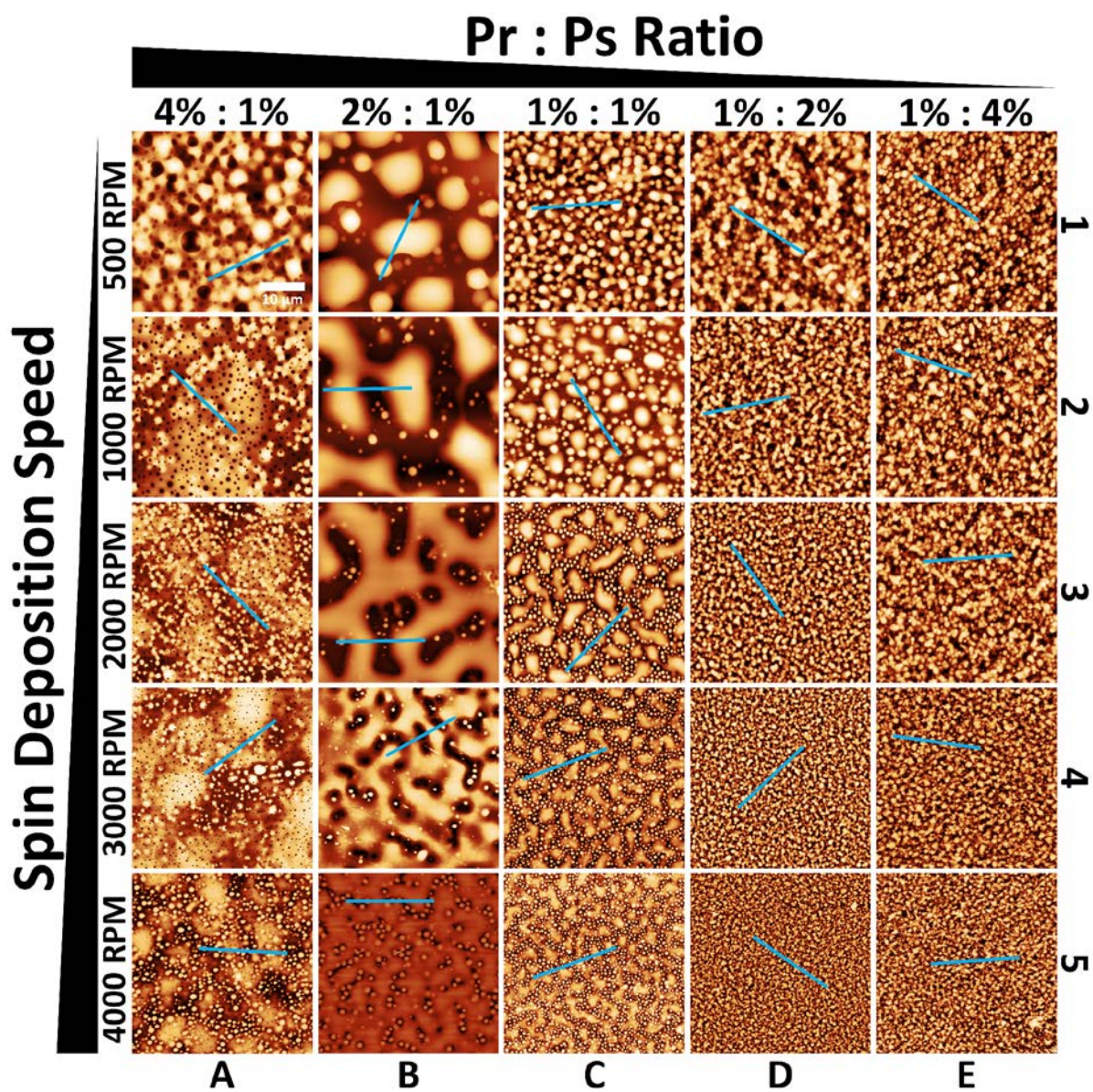
210 Phase separation in polymer blend systems is the development of two distinct regions (phases)
211 of polymers from an initially homogenous solution. Similar to oil and water, polymers which
212 are incompatible separate from one another. Dissolving biopolymers in an acid protonates the
213 polymer chains, promoting segregative phase separation.[15] Upon separation, topographical
214 features develop as the film dries as the system attempts to minimize surface energy. Typically,

215 spheres or pores are formed as they have the lowest surface area to volume ratio. These features
216 grow as the system continues to minimize total surface energy. [44], [45]

217 **Figure 1** shows AFM images of BSA-Ch blend films. High resolution images each blend are
218 provided in **Figure S2 – S6**, with accompanying line profiles provided in **Figure S7 – S11** in
219 Supporting Information). Pores formation in the 4:1 and 2:1 BSA-Ch blend formed through
220 different mechanisms. Pores are discussed in the supplementary information.

221 In the 4:1 BSA-Ch blend, increased spin speed inhibited protuberance (spherical bumps)
222 growth, resulting in smaller, more homogeneously dispersed spheres. Feature diameter and
223 density data (represented as mean \pm standard deviation, **Figure 2** and **Figure S12**) shows
224 increased spin speed decreased protuberance diameter, and increased protuberance number per
225 area (protuberances/ μm^2). This follows the general trend observed for all films. Mean
226 protuberance diameter decreased from 2.91 μm (500 rpm) to 0.81 μm (4000 rpm) (**Figure 1**,
227 A1 – A5). The 4:1 BSA-Ch blend was the only blend to contain salami structures $\geq 50 \mu\text{m}$
228 (**Figure S13** in Supporting Information). Deposition at 500 rpm of the 4:1 blend resulted in
229 dewetting, attributed to the feature length approaching film thickness.[17] This is known to
230 occur during the latter stages of, and interfere with, phase separation. Low spin speeds when
231 casting films allows more time for phase separation to occur, causing feature diameter to
232 exceed film thickness (**Figure S12**, **Figure S14** in Supporting Information), leading to the
233 salami structure. The discontinuous salami domain is composed entirely of protuberances.
234 Pores are localised outside perimeter of the salami domains. The formation of the salami
235 morphology at this blend ratio may explain the variation in growth mechanism compared to a
236 high polysaccharide content blend (see below). This indicates that pores within the BSA
237 domain (and protuberances contained within the discontinuous Ch domain) are controlled by a
238 secondary phase separation process, which is consistent with our observations of film thickness
239 [17], [46]. Lastly, in the 4:1 blend, higher spin coating speeds resulted in thinner samples, as

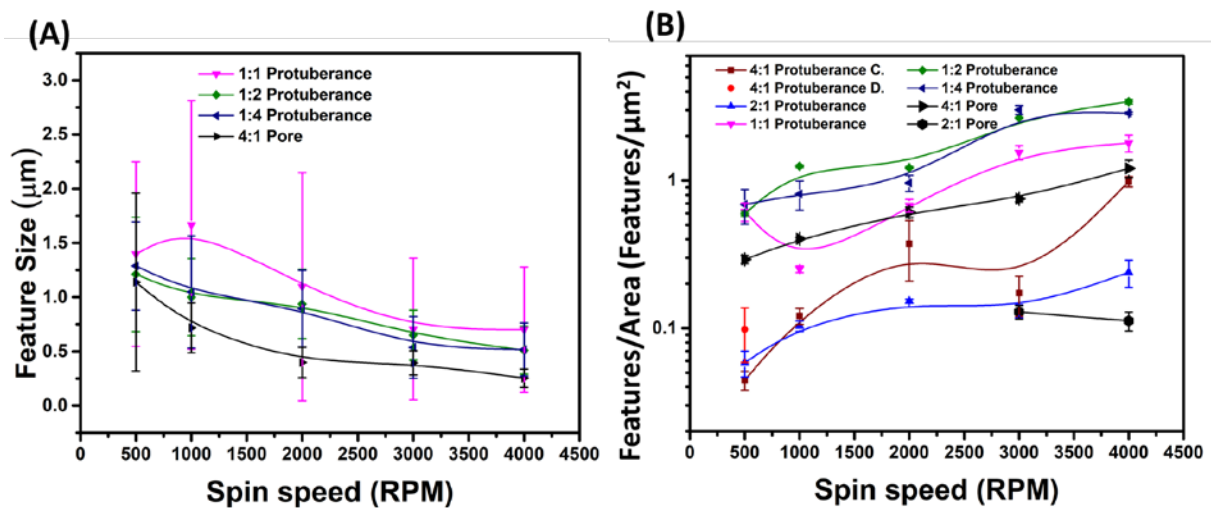
240 did blend solutions with lower viscosity (lower w/v% solutions, **Figure S14** in Supporting
241 Information for further details).



242
243 **Figure 1:** AFM image grid showing results of casting thin-films at 65 % relative humidity from
244 specific Pr-Ps (protein-polysaccharide) solutions of BSA-Ch-FA at various spin speeds. Each
245 image is $40\ \mu\text{m} \times 40\ \mu\text{m}$ area (scale bar $10\ \mu\text{m}$, shown in 4:1 blend at 500 rpm). In the image,
246 bright areas are higher and dark areas are lower. Line profile (blue lines) may be found in
247 each image and its corresponding **Figure S2 – S6** in Supporting Information. Column A = 4
248 w/v% BSA and 1 w/v% Ch (4:1), column B = 2 w/v% BSA and 1 w/v% Ch (2:1), column C =

249 1 w/v% BSA and 1 w/v% Ch (1:1), column D = 1 w/v% BSA and 2 w/v% Ch (1:2), column E
 250 = 1 w/v% BSA and 4 w/v% Ch (1:4). Row 1 = 500 rpm, row 2 = 1000 rpm, row 3 = 2000 rpm,
 251 row 4 = 3000 rpm and row 5 = 4000 rpm.

252 At all spin speeds, protuberances follow a general trend of decreasing mean diameter with
 253 increasing spin speed (**Figure 2a**). As a result, BSA-Ch blend film root-mean-squared (RMS)
 254 roughness of the films and surface area ratio (%) decreases with increasing spin speed,
 255 discussed in more detail the Supporting Information (**Figure S15**). As protuberances are the
 256 desired morphology, a simple, predictable and efficient method of controlling feature diameter
 257 like this is highly advantageous.



258
 259 **Figure 2:** Statistical analysis of BSA-Ch blends for feature diameter and feature number/area.
 260 All but the 4:1 blend refers to protuberance measurements, with the 4:1 and 2:1 blend data
 261 displaying both protuberance and pore data separately. The circular legend for the 4:1 blend
 262 refers to feature diameter in the discontinuous domain, i.e. salami structure regions. **A)** Refers
 263 to feature diameter plotted against spin speed while **B)** details features/µm² vs spin speed for
 264 4:1, 2:1, 1:1, 1:2 and 1:4 blends respectively.

265

266 **Figure 1** Column B contains the most visually distinct film structures, with the largest
267 protuberances of any blend formed. **Figure 1**, B1 and B2, show that increasing the film casting
268 spin speed of 2:1 BSA-Ch blends reduced mean protuberance diameters from 2.91 μm (500
269 rpm) to 1.60 μm (1000 rpm). The same increase in rpm also narrowed protuberance size
270 distribution (SD), from 1.5 μm – 6.1 μm to 0.7 μm – 3.2 μm . Spin speeds above 2000 rpm
271 produced a mixed porous/protuberant (**Figure 1**, B3 – B5). Protuberance diameter decreases
272 from 1000 rpm to 3000 rpm (1.6 μm to 0.81 μm). This reduction in protuberance diameter is
273 less than the initial reduction from 500 to 1000 rpm (**Figure 1**, B2 – B4). Protuberance mean
274 diameter increases at 4000 rpm (**Figure 1**, B5) to 0.99 μm . The increase in mean diameter is
275 likely due to shear at high speeds, as increased speeds should remove solvent quicker,
276 inhibiting growth. Spin speed thereby reduces the diameter of protuberances through faster
277 solvent evaporation and create larger ovoid protuberances (non-spherical protuberances
278 elongated on one axis) through shear forces, similar to the pore effect described in the 2:1 blend
279 [18]. The number of protuberances per area increased linearly from 500 rpm to 4000 rpm with
280 increased spin speed (**Figure 2b**). The submicron features in **Figure 1** are smaller than most
281 biopolymer blends in the literature (typically 10 μm in diameter and above). We attribute our
282 smaller features to the chosen biopolymers, spin speed, and chosen solvent.[12]

283 Solvents likely play a large role in forming the large features typically associated with
284 biopolymer thin-films morphologies and other structures produced from biopolymer blends.
285 Slowly evaporating blends produce large scale features.[23]:[47] Low vapour pressure (non-
286 volatile) solvents evaporate slowly, while high vapour pressure (volatile) solvents evaporate
287 quickly producing smaller feature sizes.[47]:[48] This may explain why biopolymer blends
288 produce large features, as water is the typical solvent. [12], [49]–[51] De Jong & van de Velde
289 segregatively phase separated whey protein/polysaccharide blends using water. Features were
290 5 – 10 μm in size.[12] PS/PEG blends use toluene, which is much more volatile than water,

291 producing features 200 – 400 nm in diameter.[40] Furthermore, using toluene as a solvent (less
292 volatile) produces larger features than chloroform (more volatile).[47]

293 When the quantities of protein and polysaccharide are approximately equal (1 w/v% BSA
294 to 1 w/v% Ch (**Figure 1**, Column C)) an intermediate state is seen, where larger, coalesced
295 features are observed, but a continuous phase is not sufficiently formed. Protuberance diameter
296 initially increases from approx. 1.40 μm to 1.67 μm with spin speed increase from 500 to 1000
297 rpm (**Figure 2a**). This is in conjunction with a sharp decrease in protuberances per area (**Figure**
298 **2b**) suggesting a growth process. From 1000 rpm to 4000 rpm (**Figure 1**, C2 – C5),
299 protuberance diameter decreases from 1.67 μm to 0.71 μm , while the number per area increases
300 (**Figure 2b**). This data shows that reducing the time for solvent loss produces smaller
301 protuberances and that there is a large degree of control over pattern formation. However,
302 above 1000 rpm protuberances are more irregular and less circular in shape. While the 1:1
303 BSA-Ch blend produces smaller protuberances than previously discussed blends, higher speeds
304 introduce an undesired pattern inhomogeneity. Increasing spin-coating speed from 2000 rpm
305 to 4000 rpm results in increased average diameter of these irregular protuberances (2.6 – 6.0
306 μm). These features appear similar to high spin speed 2:1 blends (**Figure 1**, B2 – B5). The
307 1:1 blend at 2000 rpm (**Figure 1**, C3) adopts a morphology similar to 2:1 blend at 1000 rpm
308 (**Figure 1**, B2) with larger protuberances interconnecting to form irregularly shaped ovoids.
309 3000 rpm (**Figure 1**, C4) produces flatter, larger, more branched features, similar to 2:1 BSA-
310 Ch blends at 2000 rpm (**Figure 1**, B3). This effect is further exaggerated at 4000 rpm (**Figure**
311 **1**, C5). We attribute this to higher shear stresses on larger structures at higher spin speeds.

312

313 Reduction of the BSA ratio from 2:1 to 1:1 (**Figure 1** Column C, **Figure S4**) results in
314 insufficient protein quantity to form a continuous phase as in **Figure 1** B3, *i.e.* phase inversion

315 does not occur preventing the pseudo pores seen in the 2:1 blend. This indicates that high
316 protein concentration is required for pore formation. The reduction of protein content to 1
317 w/v% produced a more monodisperse sample, and provided smaller feature diameters than 2:1
318 and 4:1 BSA-Ch blends, both desirable traits for patterning surfaces. Equally, the reduced BSA
319 content produced smaller protuberances, as did higher spin speeds. Complicating things
320 further, spin speeds above a certain maximum elongate the larger structures on the surface; that
321 maximum is blend dependant. The reduction of BSA w/v% (in contrast to the 2:1 and 4:1
322 blends) produces smaller BSA domains as less material is present to form these domains.
323 While mean diameter reduces with increased spin speed, larger domains increase in diameters
324 under shear with increased spin speed. Never-the-less, the 1:1 BSA-Ch blend results
325 demonstrate the ability to easily control feature diameters and features/area. This is vital for
326 maximising applicability. Use of patterned biopolymer films in a broad range of applications
327 necessitates the ability to produce an equally broad range of features diameters and
328 frequencies.[33]

329

330 1:2 (**Figure 1**, Column D and **Figure S5**) and 1:4 blends (**Figure 1**, Column E and **Figure S6**)
331 follow the simplest, and near identical, trends. Protuberance diameter decreases linearly while
332 increasing spin speed for both blends, with diameters generally smaller for the 1:2 BSA-Ch
333 blend. Mean protuberance diameter ranges from 1.21 - 0.51 μm for 1:2 blends compared to
334 1.29 - 0.52 μm for 1:4 blends, with spin speeds increased from 500 to 4000 rpm. Both the 1:2
335 and 1:4 blends show feature diameters smaller than 1:1, 2:1 and 4:1 blends. The increased
336 concentration of the continuous phase (Ch) increases viscosity, limiting coalescence thereby
337 reducing feature diameter.[33] The primary differences lie in the histograms for both blends,
338 with the 1:4 blends showing better defined peaks at higher spin speeds, indicating inhibited

339 growth.[52] Both blends exhibit little growth in protuberances per area until a large increase
340 is observed from 2000 - 3000 rpm (**Figure 2b**). This demonstrates that biopolymer blends may
341 be treated the same way as traditional polymer blends, meaning biopolymer blends can be
342 processed with pre-established techniques. Further, this method of producing a patterned
343 surface with biopolymer blends is much quicker than previously discussed techniques, and
344 produces features of approximately 1 μm .^[34] This is much smaller than other bottom-up
345 biopolymer techniques, and is similar to blends produced with synthetic polymers [40], [53]–
346 [57].

347

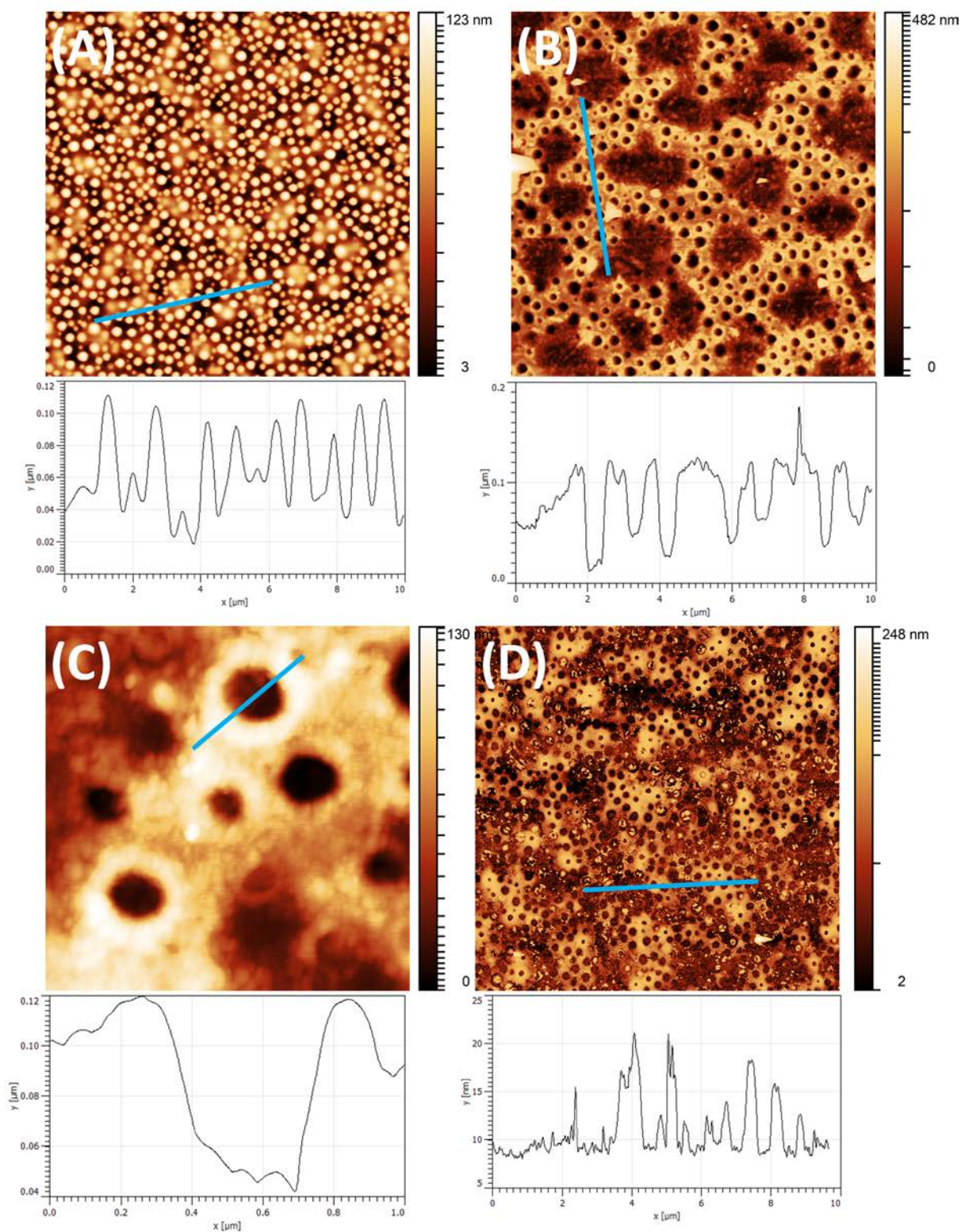
348 *Chemical characterisation of BSA-Ch blend films*

349 Immersing coated substrates in a basic aqueous solution selectively dissolves the readily water-
350 soluble BSA. This allows for selective removal of the protein. **Figure 3a** shows a neat the 1:1
351 BSA-Ch blend, while **Figure 3b** shows both the large and small BSA domains removed from
352 the Ch matrix. Line profile analysis shows that larger domains do not penetrate directly to the
353 substrate, but are suspended in the Ch matrix. Smaller spherical domains protrude much deeper
354 into the Ch domain confirming late stage dewetting. Many of the pores in **Figure 3b** contain
355 extruded rims extending from the surface, producing a crater shape. This provides insight into
356 the protuberances formation mechanism. Coalescence of droplets is generally broken into four
357 steps: (i) droplet approach, (ii) matrix drainage between droplets, (iii) breakup of the matrix
358 film and (iv) relaxation of coalesced droplet into spherical shape.^{[58]–[60]} Drainage of the Ch
359 matrix is observed in smaller BSA protuberances in contact with larger BSA domains.
360 However, many pores retain this crater morphology (**Figure 3c**). Other work on polymer
361 blends has shown these sharp, elevated rims occur when the continuous phase climbs around
362 the discontinuous droplets, *i.e.* pinning of the triple-phase protein-polysaccharide-air boundary,

363 droplet breakup, and resultant inhibited growth. [61], [62] Note that the features in our etched
364 BSA-Ch blend are over thirty times smaller than those of polystyrene/poly(methyl
365 methacrylate) blends, and are equivalent to polyfluorene blends. This was seen in other blends
366 (**Figure S16** in Supporting Information) with rim height approx. 40 nm.

367 When using BCPs to pattern metals, metal is incorporated into a single domain due to
368 the different chemistries of each BCP block.[63] Ch is well known for its metal binding
369 capacity, due to the free electron pair on the amino group.[64]–[67] FeCl₃ was chosen as the
370 metal incorporate, as the amino group of Ch will chelate hard cations such as Fe³⁺. [68] Unlike
371 Ch, BSA binds to soft metal cations.[37] FeCl₃ was chosen as the metal incorporate for a
372 second reason. Metal anions can promote, or inhibit, the binding of metal cations to proteins.
373 In particular, the Cl⁻ anion has a low affinity for BSA, as it is weakly hydrated. This effect is
374 described by the Hofmeister series.[69], [70] By choosing FeCl₃ as the metal precursor, both
375 the hard nature of the metal cation, and weakly hydrated nature of the metal counter-anion,
376 ensure that metal is incorporated only into the Ch domain. This allows for identification of the
377 Ch phase. Water was not chosen as a solvent for FeCl₃, as BSA is soluble in water. Using
378 water as a solvent for metal incorporation would result in the solubilization (and removal) of
379 BSA during the metal incorporation step, interfering with the identification of the Ch phase.
380 The use of anhydrous EtOH ensures the BSA domain is not solubilized. Though the number
381 of factors considered may seem excessive, trying to incorporate metal into a singular
382 biopolymer domain is no small feat. **Figure 3d** confirms that the continuous phase is Ch due
383 to the Fe₃O₄ uptake mirroring the BSA-Ch blend. Large BSA ovoid protuberances are reflected
384 as large irregularly shaped voids (large areas absent of metal uptake) in **Figure 3d**. Smaller
385 BSA protuberances are reflected as circular pores in the metallic film. Both the BSA etch and
386 metal incorporation do not reveal the bottom silicon substrate, indicating a thin layer of Ch
387 separates the BSA droplets from the substrate, blocking the Si surface, a feature observed in

388 almost all polymer blends.[53] Any application this may have as a hard mask would require
389 perforation of the BSA domain to the Si substrate, as the Si must be accessible to the etchant.
390 To the best of our knowledge, purely lateral phase separation of a polymer blend has only been



392

393 **Figure 3:** AFM images and surface profiles of 1:1 BSA-Ch blends, 3000 rpm on planar silicon

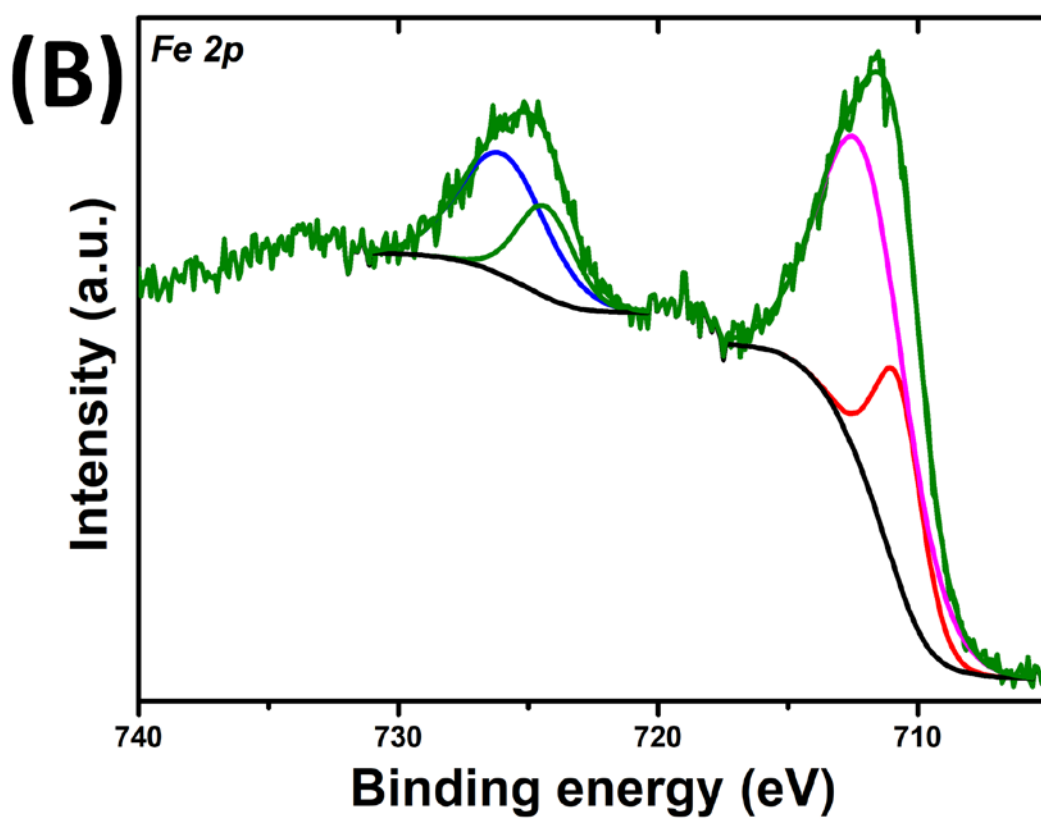
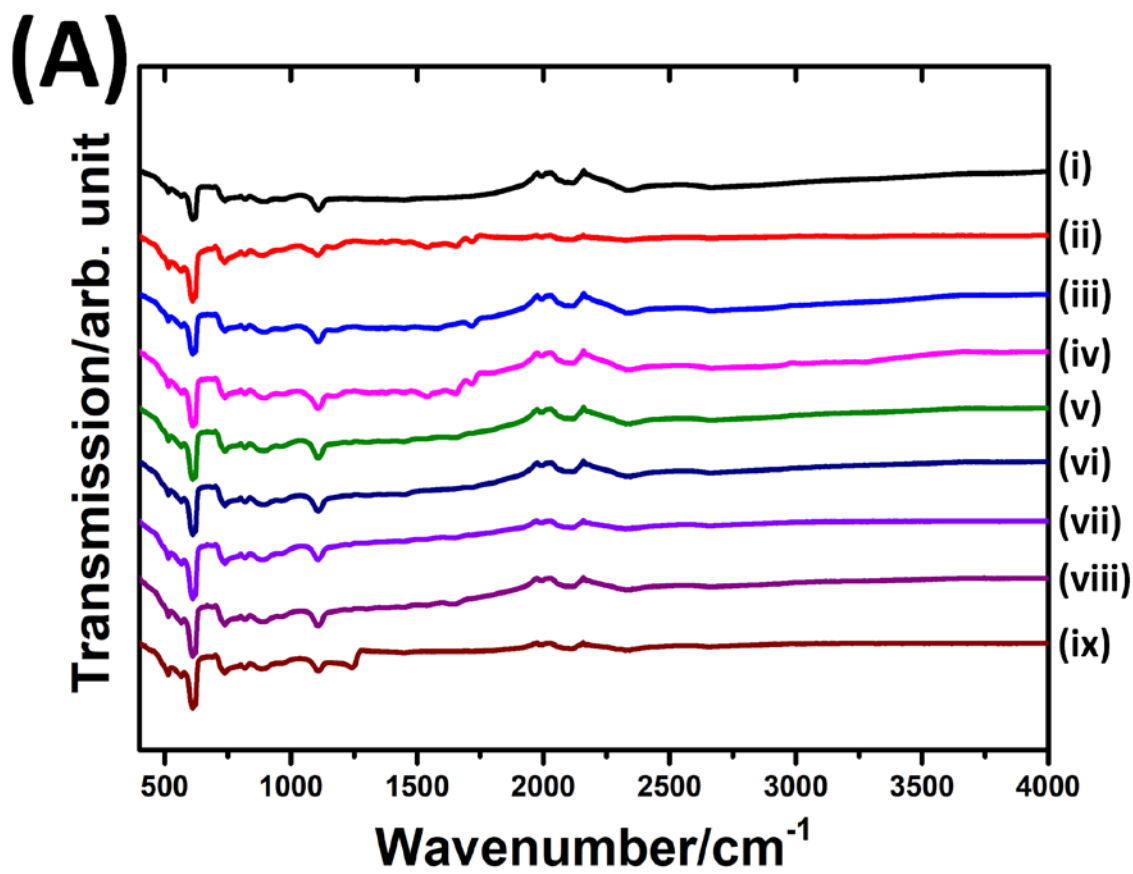
394 substrates. A) Refers to blend before Tris-HCl etch. B) Refers to blend post selective etching.

395 C) Enhanced view of selectively etched BSA domains demonstrating extruded rim structure in
396 Ch film. D) Refers to blend post selective metal incorporation and calcination.

397 **Figure 4A** shows FTIR transmission spectra of the biopolymer blend after various
398 processes. This was done to confirm chemical changes in the sample after BSA removal,
399 crosslinking, and calcination. For clarity of comparison, a bare Si wafer, plain BSA, and plain
400 Ch were analysed so that their identifying peaks could be differentiated from any unique to the
401 blend films. The bare Si wafer (**Figure 4A**, spectra i) has standard identifying peaks at 514 (Si–
402 O deformation)[71], 611 (Si–Si bond vibrations in the bulk)[72], 739 (O–H out of plane
403 bending)[71], 891 (Si–O–H mode due to oxidation of upper silicon layer)[72] and 1108 cm⁻¹
404 (Si–O–Si asymmetric stretching).[73] The shape and intensity of these peaks are similar for
405 all samples. The neat BSA film spectrum (**Figure 4A**, spectra ii) contained a weak band at
406 1376 cm⁻¹ due to CH₃ symmetric bending.[74] The amide I, and amide II modes of BSA were
407 observed at 1656 cm⁻¹ and 1544 cm⁻¹ respectively.[74] The amide II' transmission band is seen
408 at 1448 cm⁻¹. [75] The peak at 3208 cm⁻¹ can be assigned to asymmetric and symmetric H–O–
409 H stretching, resulting from residual water in the film after casting.[74] Peaks in the Ch spectra
410 (**Figure 4A**, spectra iii) are observed at 1718 cm⁻¹, 1573 cm⁻¹ and 1374 cm⁻¹ corresponding to
411 the amide I, amide II, and amide III bands, respectively.[74], [76], [77] The peak at 1445 cm⁻¹
412 can be assigned to an N-H bending of Ch. [78], [79]

413 The 1:1 blend (**Figure 4A**, spectra iv) exhibited no new peaks indicating no new bonds
414 occur. The Amide II peak for the non-crosslinked BSA film and the non-crosslinked Ch film
415 becomes less prominent after crosslinking (**Figure 4A**, spectra v and vi). This indicates a
416 reduction in free amines after crosslinking and the formation of a Schiff base.[80] After
417 crosslinking, the 1:1 BSA-Ch blend (**Figure 4A**, spectra vii) has a peak at 3264 cm⁻¹: this is
418 due to water retained in the film after nitrogen drying. The crosslinked 1:1 film's amide II

419 peaks are less prominent post crosslinking, confirming crosslinking occurred. As the peaks
420 appear similar to those in the neat biopolymer films after crosslinking, we can infer only
421 intramolecular crosslinking has occurred which would suggest no BSA remains on the film
422 after etching. This is expected as BSA is segregated from the Ch domain. However, some
423 small degree of intermolecular crosslinking may occur at the BSA-Ch interface, though this
424 may be below the detection limit of the machine.[10]



426 **Figure 4:** A) FTIR spectra of **i)** bare silicon wafer, **ii)** 1 w/v% BSA film 3000 rpm deposition,
427 **iii)** 1 w/v% Ch film 3000 rpm deposition, **iv)** 1:1 BSA-Ch blend film 3000 rpm deposition, **v)** 1
428 w/v% BSA film 3000 rpm deposition crosslinked, **vi)** 1 w/v% Ch film 3000 rpm deposition
429 crosslinked, **vii)** 1:1 BSA-Ch blend film 3000 rpm deposition crosslinked, **viii)** 1:1 BSA-Ch
430 blend crosslinked film after Tris-HCl etch and **ix)** porous iron oxide matrix after annealing and
431 calcination treatment. **B)** Shows the XPS Fe 2p spectra of iron porous matrix after annealing
432 and calcination treatment.

433 The spectra of the etched film (**Figure 4A**, spectra viii) after crosslinking retains the BSA
434 peaks. This suggests residual BSA on the surface due to intermolecular crosslinking, or after
435 washing. Calcination of the BSA-Ch blend after metal incorporation results in a spectra with
436 no characteristic peaks of BSA or Ch, indicating their removal (**Figure 4A**, spectra ix). The
437 more prominent Si–O–Si band at 1108 cm^{-1} after calcination indicates a thicker oxide layer
438 than the native oxide of the original Si wafer. This is further confirmed by the peak in the bare
439 Si wafer (1237 cm^{-1}) shifting to 1245 cm^{-1} , which occurs when oxide thickness increases, a
440 consequence of the long calcination time and high temperature required to ensure complete
441 biopolymer removal.[81] This peak corresponds to the longitudinal optical phonon of SiO_2
442 (LO) around 1250 cm^{-1} , which occurs in thermal oxides.[82] Fe peaks were not observed at
443 630 cm^{-1} or 540 cm^{-1} , characteristic of magnetite and hematite respectively. FTIR confirmed
444 successful crosslinking of the biopolymer film before etching and successful removal of the
445 biopolymers after calcination.[83]

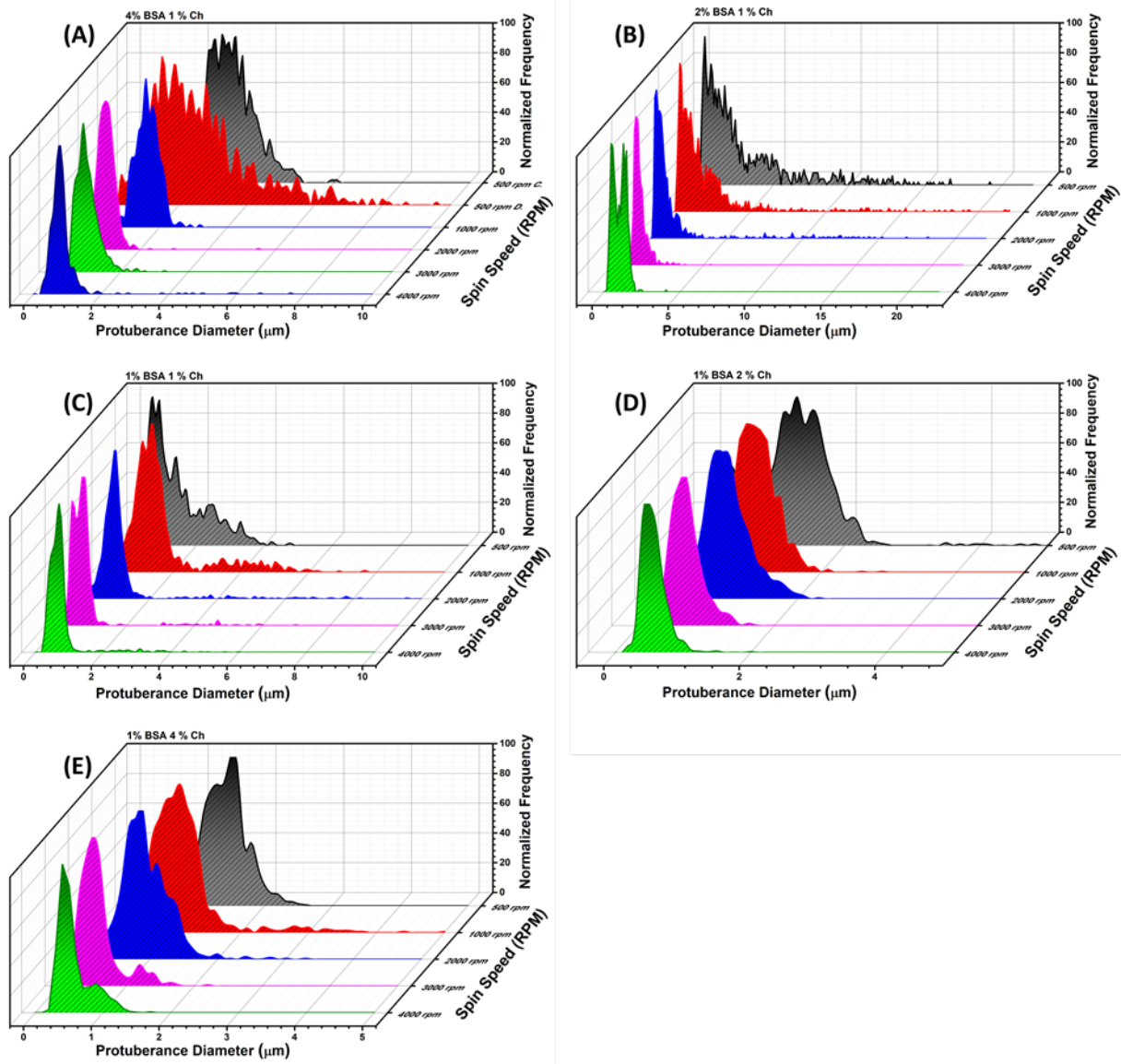
446 XPS was used to determine whether the iron present was predominantly hematite or
447 magnetite to confirm metal incorporation and oxidation (**Figure 4B**). The chemical
448 composition of the iron oxide matrix before/after annealing and calcination was confirmed by
449 Fe 2p XPS studies. Following calcination, the Fe 2p core level spectrum (see **Figure 4B**)

450 consists of two sharp peaks at 711.6 eV (Fe 2p_{3/2}) and at 725.7 eV (Fe 2p_{1/2}) which are
451 broadened due to the presence of Fe²⁺ and Fe³⁺ ions. Curve-fitting using Gaussian–Lorentzian
452 line shapes provides individual binding energies of 710.7/724.3 eV (assigned to Fe²⁺) and
453 712.0/726.0 eV (Fe³⁺) in agreement with literature reports.[84] The Fe³⁺/Fe²⁺ ratio was
454 estimated to be approx. 2:1, typical of magnetite. The C1s peak is nominal demonstrating the
455 effective removal of biopolymeric material during calcination, and is consistent with
456 extraneous carbon species adsorbed during sample preparation (**Figure S17** in Supporting
457 Information).

458 **Protuberance Growth in Blend Thin-Films**

459 Feature diameter determines the properties of a surface, such as pattern transferability,
460 hydrophobicity, etc. SDs can be used provide insight into film features and their growth
461 mechanisms[52]. This allows control of feature formation to optimise films for specific
462 applications. Protuberance diameter data was extracted from AFM images and presented as
463 SDs in normalized frequency histograms (**Figure 5**). Information about pore diameter and
464 mechanism of pore formation can be found in the Supporting Information (**Figure S18**). All
465 blends exhibit multimodal SDs with protuberances of large diameter at low spin speeds.
466 Increasing spin speed reduces the number of modes and shifts population weight to narrower
467 diameters, further indicating a nucleation and growth process. This also indicates that faster
468 spin speeds, up to certain thresholds, produce more homogeneously distributed features of more
469 uniform diameter. This is crucial to production of effective patterned thin films. The 2:1 BSA-
470 Ch blend at 4000 rpm (**Figure 5b**) is an exception to the above, exhibiting a bimodal SD with
471 peaks at 1.3 μm and 1.5 μm protuberance diameters. This is likely due to shear effects at higher
472 spin speeds.

473



474

475 *Figure 5: Statistical analysis of BSA-Ch blends for protuberances and frequency of*

476 *protuberance sizes. Each curve based on approx. 1000 protuberance diameter measurements.*

477 *All but the 4:1 blend refers to protuberance measurements contained within the matrix, with*

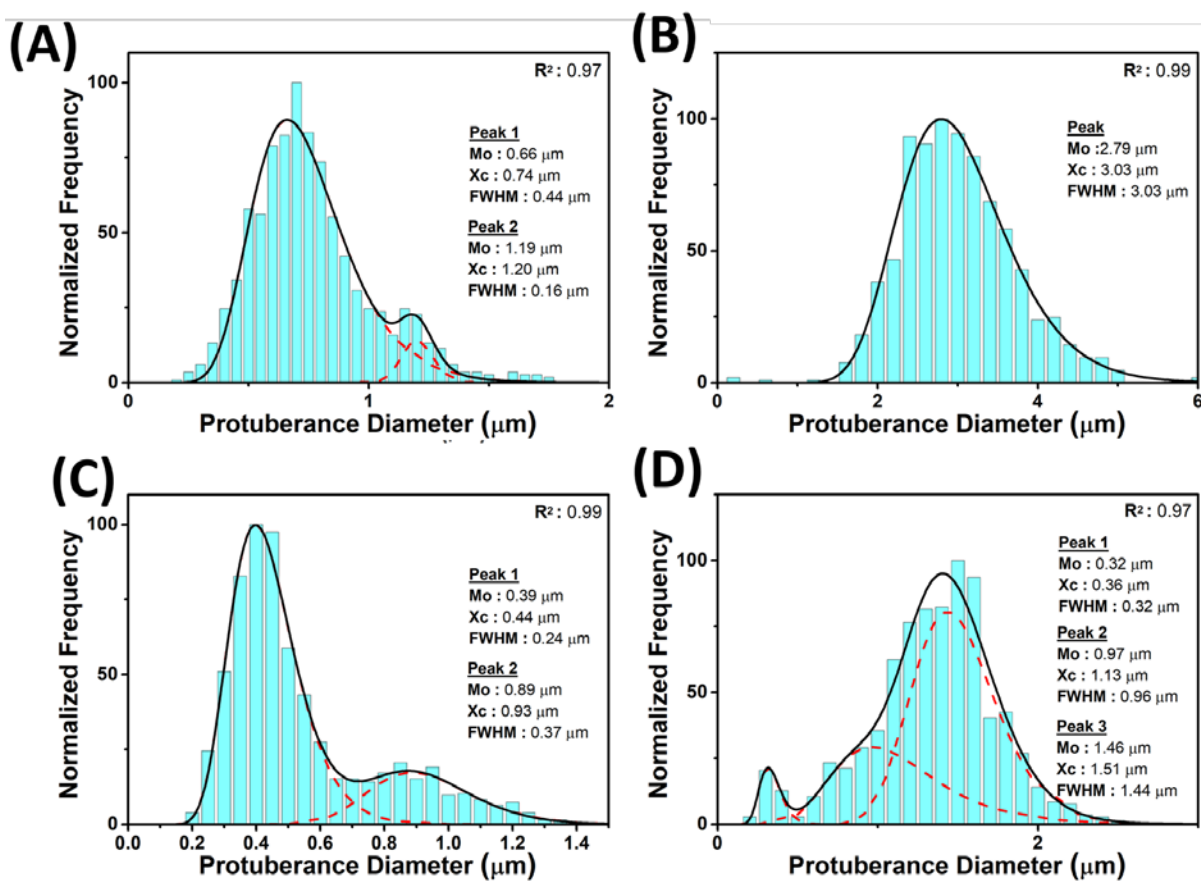
478 *the 4:1 blend data displaying protuberance data for the continuous and discontinuous (salami*

479 *structure) domain. A – E displays feature frequency vs diameter of observed features for 4:1,*

480 *2:1, 1:1, 1:2 and 1:4 blends respectively.*

481

482 Ostwald ripening occurs by the transfer of material from smaller features to larger
 483 features by diffusion. The result is smaller μ features reducing in diameter while larger features
 484 increase in diameter.[52] This is distinct from coalescence, where multiple spherical features
 485 merge to form a larger version of the feature with lower surface area to volume ratio. Ostwald
 486 ripening results in broader SDs and is undesirable. SDs arising from these processes have
 487 distinct identifiable characteristics. Curve fitting may be used to determine the modality of the
 488 SD (either unimodal or polymodal), identify the mode diameter (Mo), and centre of gravity
 489 (Xc) of the identified peaks.[85] Typically, this includes the fitting of a lognormal curve to the
 490 SD. [52], [85]–[88] Lognormal peak fitting was achieved using the non-linear least squares
 491 method.[88], [89]



492
 493 **Figure 6:** Protuberance SD of A) 4:1 BSA-Ch blend, 4000 rpm deposition, B) 4:1 BSA-
 494 Ch blend, 500 rpm deposition, C) 1:4 BSA-Ch blend, 4000 rpm deposition and D) 1:4 BSA-Ch

495 *blend, 500 rpm deposition. The black curve (solid) denotes the best unimodal or polymodal fit*
496 *with the distribution. The deconvoluted peaks, shown in red (dashed), show the separate*
497 *populations in the SD.*

498 The 4:1 blend exhibits coalescence characteristics; increased feature diameter and peak
499 broadening corresponding to longer evaporation times (**Figure 6a** and **b**). Additionally, the
500 SD transitions from a bimodal distribution to unimodal distribution.[90] In contrast, the 1:4
501 BSA-Ch blend exhibits Ostwald ripening characteristics; feature diameter increases with
502 longer evaporation time (**Figure 6c** and **d**), but formation of an extra peak (at approx. 0.3 μm)
503 is observed with longer drying time (Peak 1, **Figure 6d**), indicating production of smaller
504 particles, characteristic of Ostwald ripening. Increasing the concentration of Ch increased the
505 continuous phases viscosity, resulting in Ostwald ripening being the dominant growth
506 mechanism.[33]

507 These results show sub-micron features may be achieved using industrial standard
508 deposition techniques. This technique produces rapid pattern realisation, without requiring
509 extensive environmental controls such as temperature or humidity regulation. Feature diameter
510 and frequency/area are substantially similar to synthetic polymer blends. This means that
511 biopolymer blends could be incorporated into existing production processes for applications
512 where biopolymers offer a distinct advantage, with all the environmental and economic benefits
513 that come with using renewable resources. Furthermore, assignment of the protein and
514 polysaccharide domain was possible due to selective etching and metal incorporation. Both
515 techniques show promise as a method of identification of each domain (inaccessible to typical
516 staining techniques at such a small scale). This is simply achieved by the use of a crosslinking
517 agent, aqueous buffer and cheap metal additive, avoiding the use of expensive or specialist
518 enzymes for identification. The attraction of these techniques is the ability to identify each

519 domain without reliance on highly sensitive surface specific methods. Furthermore, these
520 techniques compliment other facile surface probing techniques such as water contact angle
521 measurements, which show clear differences when analysing the various surfaces encountered
522 **(Figure S19)**. Though incorporation and etching provides insight into the internal structure
523 (and thereby formation mechanism) of the film, they do little to inform us of the chemical state
524 of the crosslinked blend at the interface. Higher sensitivity ATR-FTIR would be required to
525 determine if crosslinking occurs at the interface. Deconvolution of the SD clearly shows the
526 presence of 2 growth mechanisms (Ostwald ripening and coalescence). Understanding of the
527 growth mechanisms is invaluable when choosing protein:polysaccharide ratios for surface
528 patterning. Selective incorporation of a metal salt could further be enhanced by use of other
529 metal salt derivatives, varying weight percentage of the salt type or varying contact time with
530 the blend film. It would be interesting to see if other salts could show preference to the protein
531 domain when incorporating into the blend film.

532

533 **Conclusion**

534 Spin speed and blend ratio are major factors when determining feature diameter, growth
535 mechanism and morphology. Blends generally showed a decrease in feature diameter and
536 roughness, while increasing in features per area with increasing spin speeds and polysaccharide
537 content. Faster drying times (high spin speeds) generally resulted in smaller features, while
538 longer drying times (low spin speeds) resulted in larger features. Simply put, faster spin speeds
539 increase the evaporation rate, limiting the amount of time features have to grow. Increasing
540 viscosity by increasing the relative Ch ratio reduced feature diameter due to lowered polymer
541 mobility. As Ch content is increased, it creates a viscous, honey-like matrix in which BSA
542 domain growth is hindered. Faster spin speeds resulted in more monodisperse blend SD's,

543 unless banding occurred due to shear effects at high speed. Protein:polysaccharide ratio played
544 an important role in determining morphology. Increasing the relative BSA ratio resulted in
545 larger BSA domains, and banding of the BSA domain at high shear due to the difference in
546 viscosity between the two phases.[18] Selective etching and selective incorporation of the
547 metal salts in the Ch domain allowed for protuberances to be assigned as the BSA domain, a
548 first for biopolymer blends. Coalescence was inhibited in 1:4 BSA-Ch blends due to the
549 increased viscosity of the blend, with feature growth described by Ostwald ripening. 4:1 blends
550 grew by a coalescence mechanism. 1:2 and 1:4 BSA-Ch blends have the smallest circular
551 protuberances. This is attributable to the blend solutions high viscosity and low amount of
552 BSA to form a discontinuous phase. The 1:1 blend smaller, circular features decrease in
553 diameter, while larger ovoid features increase in diameter at higher spin speeds (i.e. high shear).
554 This shows inhibited growth of the film morphology at higher spin speeds, and (similar to the
555 2:1 blend at 1000 rpm) an attempt to phase invert its morphology. Porous films are formed in
556 the 4:1 BSA-Ch blend. Pores decrease in diameter with increasing spin speed. Pores are
557 produced from a solvent rich phase. The 2:1 blend phase inverts at high spin speeds. After
558 phase inversion, pores increase in diameter with increasing spin speed due to high shear
559 elongating their domains.

560 This work demonstrates that protein-polysaccharide blends can be used to rapidly produce
561 biopolymer thin films with sub-micron patterns, all without requiring extracting, refinement
562 and production of synthetic polymer precursors. Due to their patterns, these unique biopolymer
563 thin-films present a vast spectrum of possible applications. These range from simple
564 applications including traditional packaging alternatives and smart foods production, to more
565 complex applications such as hydrophobic textile coatings, lithographic templates,
566 antireflective coatings, and state-of-the-art hierarchal designs used in biomedicine or
567 responsive membranes.[22], [33] Feature growth mechanisms were identified through analysis

568 of the SD. We did not find any previous attempts into the literature to determine the growth
569 mechanism, which may be one reason biopolymer blends thus far have had such large feature
570 diameters. Not only do these blends use environmentally benign and economically cheap
571 biopolymers, but they have feature diameters on a scale with those of synthetic polymer blends,
572 while utilizing industrially viable methods. This bottom-up method allows for instant pattern
573 production without the need for complex equipment and techniques such as e-beam
574 lithography. Patterns may be produced using benchtop equipment, without the long annealing
575 times associated with synthetic polymers. Biopolymer blends are projected to play a pivotal in
576 future manufacturing of biomedical, electronic, sensor and optical components. [22], [32], [33]
577 Research of into the properties of biopolymer blends thin-film surface morphologies is an
578 emerging field, and our method for producing these blends in a controlled manner is a
579 progressive step in the adoption of these films in modern technologies.

580 **Acknowledgements**

581 Dr. Joseph Tobin and Richard Curly of Glantreo Ltd., Ireland, Dr. John O’Connell of the
582 Materials Chemistry and Analysis Group, University College Cork, Cork, Ireland. The Irish
583 Research Council for Science, Engineering and Technology is also acknowledged for financial
584 support of the work.

585

586 **Supporting Information Available:**

587

588 **References**

- 589 [1] OECD, “Future Technology Trends,” in *OECD Science, Technology, and Innovation*
590 *Outlook, 2016*, 2016, pp. 77–125.
- 591 [2] A. B. López, J. C. De La Cal, and J. M. Asua, “Highly Hydrophobic Coatings from

- 592 Waterborne Latexes,” *Langmuir*, vol. 32, no. 30, pp. 7459–7466, 2016.
- 593 [3] P. Mokarian-Tabari *et al.*, “Large Block Copolymer Self-Assembly for Fabrication of
594 Subwavelength Nanostructures for Applications in Optics,” *Nano Lett.*, vol. 17, no. 5,
595 pp. 2973–2978, May 2017.
- 596 [4] E. Alizadeh-Birjandi and H. P. Kavehpour, “Plant leaves icephobicity,” *J. Coatings
597 Technol. Res.*, 2017.
- 598 [5] Y. F. Fu, C. Q. Yuan, and X. Q. Bai, “Marine drag reduction of shark skin inspired riblet
599 surfaces,” *Biosurface and Biotribology*, vol. 3, no. 1, pp. 11–24, 2017.
- 600 [6] D. Borah, S. Rasappa, R. Senthamaraikannan, J. D. Holmes, and M. A. Morris, “Tuning
601 PDMS brush chemistry by UV-O₃ exposure for PS-b-PDMS microphase separation and
602 directed self-assembly,” *Langmuir*, vol. 29, no. 28, pp. 8959–8968, 2013.
- 603 [7] J. C. Blackstock, “Carbohydrates,” in *Guide to Biochemistry*, 1st ed., J. C. Blackstock,
604 Ed. Glasgow: Butterworth-Heinemann, 1989, pp. 20–31.
- 605 [8] R. L. Whistler, “Solubility of Polysaccharides and Their Behavior in Solution,” in
606 *Carbohydrates in Solution*, 1st ed., Horace S. Isbell, Ed. Amer Chemical Society, 1973,
607 pp. 242–255.
- 608 [9] M. C. García, “Drug delivery systems based on nonimmunogenic biopolymers,” in
609 *Engineering of Biomaterials for Drug Delivery Systems*, 1st ed., A. Parambath, Ed.
610 Swanston, Cambridge: Woodhead Publishing, 2018, pp. 317–344.
- 611 [10] X. Ma *et al.*, “A Biocompatible and Biodegradable Protein Hydrogel with Green and
612 Red Autofluorescence: Preparation, Characterization and In Vivo Biodegradation
613 Tracking and Modeling,” *Sci. Rep.*, vol. 6, p. 19370, May 2016.
- 614 [11] D. R. Picout and S. B. Ross-Murphy, “Rheology of Biopolymer Solutions and Gels,”
615 *Sci. World J.*, vol. 3, pp. 105–121, Mar. 2003.

- 616 [12] S. de Jong and F. van de Velde, “Charge density of polysaccharide controls
617 microstructure and large deformation properties of mixed gels,” *Food Hydrocoll.*, vol.
618 21, no. 7, pp. 1172–1187, 2007.
- 619 [13] N. A. Gengec, U. Cengiz, and H. Y. Erbil, “Superhydrophobic
620 perfluoropolymer/polystyrene blend films induced by nonsolvent,” *Appl. Surf. Sci.*, vol.
621 383, pp. 33–41, Oct. 2016.
- 622 [14] P. Xavier, P. Rao, and S. Bose, “Nanoparticle induced miscibility in LCST polymer
623 blends: critically assessing the enthalpic and entropic effects,” *Phys. Chem. Chem.*
624 *Phys.*, vol. 18, no. 1, pp. 47–64, Dec. 2016.
- 625 [15] F. van de Velde, E. H. A. de Hoog, A. Oosterveld, and R. H. Tromp, “Protein-
626 Polysaccharide Interactions to Alter Texture,” *Annu. Rev. Food Sci. Technol.*, vol. 6, no.
627 1, pp. 371–388, Apr. 2015.
- 628 [16] M. F. Butler and M. Heppenstall-Butler, “Phase separation in gelatin/dextran and
629 gelatin/maltodextrin mixtures,” *Food Hydrocoll.*, vol. 17, no. 6, pp. 815–830, Nov.
630 2003.
- 631 [17] A. Hirose, K. Shimada, C. Hayashi, H. Nakanishi, T. Norisuye, and Q. Tran-Cong-
632 Miyata, “Polymer networks with bicontinuous gradient morphologies resulting from the
633 competition between phase separation and photopolymerization †,” *Soft Matter*, vol. 12,
634 no. 6, pp. 1820–1829, 2016.
- 635 [18] B. Wolf, R. Scirocco, W. J. Frith, and I. T. Norton, “Shear-induced anisotropic
636 microstructure in phase-separated biopolymer mixtures,” *Food Hydrocoll.*, vol. 14, no.
637 3, pp. 217–225, May 2000.
- 638 [19] I. T. Norton and W. J. Frith, “Microstructure design in mixed biopolymer composites,”
639 *Food Hydrocoll.*, vol. 15, no. 4–6, pp. 543–553, Jul. 2001.

- 640 [20] H. Firoozmand and D. Rousseau, "Microstructure and elastic modulus of phase-
641 separated gelatin–starch hydrogels containing dispersed oil droplets," *Food Hydrocoll.*,
642 vol. 30, no. 1, pp. 333–342, Jan. 2013.
- 643 [21] I. C. Hoeger *et al.*, "Bicomponent Lignocellulose Thin Films to Study the Role of
644 Surface Lignin in Cellulolytic Reactions," *Biomacromolecules*, vol. 13, no. 10, pp.
645 3228–3240, Oct. 2012.
- 646 [22] N. Nady and S. H. Kandil, "Novel Blend for Producing Porous Chitosan-Based Films
647 Suitable for Biomedical Applications," *Membranes (Basel)*, vol. 8, no. 1, p. 2, Jan.
648 2018.
- 649 [23] K. Trommer, B. Morgenstern, F. Gähr, and F. Hermanutz, "SUB-MICROMETER
650 STRUCTURED TEXTILE COATINGS GENERATED FROM CELLULOSE BASED
651 POLYMER BLENDS," *Lenzinger Berichte*, vol. 87, pp. 151–161, 2009.
- 652 [24] L. Taajamaa, O. J. Rojas, J. Laine, K. Yliniemi, and E. Kontturi, "Protein-assisted 2D
653 assembly of gold nanoparticles on a polysaccharide surface †," *Chem. Commun.*, vol.
654 49, no. 13, pp. 1318–1320, 2013.
- 655 [25] P. I. C. Claro, A. R. S. Neto, A. C. C. Bibbo, L. H. C. Mattoso, M. S. R. Bastos, and J.
656 M. Marconcini, "Biodegradable Blends with Potential Use in Packaging: A Comparison
657 of PLA/Chitosan and PLA/Cellulose Acetate Films," *J. Polym. Environ.*, vol. 24, no. 4,
658 pp. 363–371, Dec. 2016.
- 659 [26] L. Taajamaa, O. J. Rojas, J. Laine, and E. Kontturi, "Phase-specific pore growth in
660 ultrathin bicomponent films from cellulose-based polysaccharides," *Soft Matter*, vol. 7,
661 no. 21, p. 10386, Oct. 2011.
- 662 [27] F. Chen, X. Monnier, M. Gällstedt, U. W. Gedde, and M. S. Hedenqvist, "Wheat
663 gluten/chitosan blends: A new biobased material," *Eur. Polym. J.*, vol. 60, pp. 186–197,

- 664 Nov. 2014.
- 665 [28] F. Chen, M. Gällstedt, R. T. Olsson, U. W. Gedde, and M. S. Hedenqvist, “A novel
666 chitosan/wheat gluten biofoam fabricated by spontaneous mixing and vacuum-drying,”
667 *RSC Adv.*, vol. 5, no. 114, pp. 94191–94200, Nov. 2015.
- 668 [29] F. Walha, K. Lamnawar, A. Maazouz, and M. Jaziri, “Rheological, Morphological and
669 Mechanical Studies of Sustainably Sourced Polymer Blends Based on Poly(Lactic Acid)
670 and Polyamide 11.,” *Polymers (Basel)*., vol. 8, no. 3, Feb. 2016.
- 671 [30] W. Cao, A. Wang, D. Jing, Y. Gong, N. Zhao, and X. Zhang, “Novel biodegradable
672 films and scaffolds of chitosan blended with poly(3-hydroxybutyrate),” *J. Biomater. Sci.*
673 *Polym. Ed.*, vol. 16, no. 11, pp. 1379–1394, Jan. 2005.
- 674 [31] C. Czibula *et al.*, “Design of Friction, Morphology, Wetting, and Protein Affinity by
675 Cellulose Blend Thin Film Composition,” *Front. Chem.*, vol. 7, no. Article 239, pp. 1–
676 10, May 2019.
- 677 [32] V. Gopishetty, Y. Roiter, I. Tokarev, and S. Minko, “Multiresponsive Biopolyelectrolyte
678 Membrane,” *Adv. Mater.*, vol. 20, no. 23, pp. 4588–4593, Dec. 2008.
- 679 [33] X. Hu, P. Cebe, A. S. Weiss, F. Omenetto, and D. L. Kaplan, “Protein-based composite
680 materials,” *Mater. Today*, vol. 15, no. 5, pp. 208–215, May 2012.
- 681 [34] R. A. Banta, T. W. Collins, R. A. Curley, P. W. Young, J. D. Holmes, and E. J. Flynn,
682 “Nanopatterned protein-polysaccharide thin films by humidity regulated phase
683 separation,” *J. Colloid Interface Sci.*, vol. 532, pp. 171–181, Dec. 2018.
- 684 [35] G. D. Jovanović, A. S. Klaus, and M. P. Nikšić, “Antimicrobial activity of chitosan
685 coatings and films against *Listeria monocytogenes* on black radish,” *Rev. Argent.*
686 *Microbiol.*, vol. 48, no. 2, pp. 128–136, Apr. 2016.
- 687 [36] M. do C. Teixeira, A. Santini, and E. B. Souto, “Delivery of Antimicrobials by Chitosan-

- 688 Composed Therapeutic Nanostructures,” in *Nanostructures for Antimicrobial Therapy:*
689 *Nanostructures in Therapeutic Medicine Series*, 1st ed., A. Ficaí and A. M. Grumezescu,
690 Eds. Elsevier, 2017, pp. 203–222.
- 691 [37] B. Saha, S. Chakraborty, and G. Das, “A Rational Approach for Controlled Adsorption
692 of Metal Ions on Bovine Serum Albumin–Malachite Bionanocomposite,” *J. Phys.*
693 *Chem. C*, vol. 114, no. 21, pp. 9817–9825, Jun. 2010.
- 694 [38] M. Oliveira, J. A. Simoni, and C. Airoidi, “Chitosan metal-crosslinked beads applied for
695 n-alkylmonoamines removal from aqueous solutions – a thermodynamic study,” *J.*
696 *Chem. Thermodyn.*, vol. 73, pp. 197–205, Jun. 2014.
- 697 [39] R. B. Hernández *et al.*, “Coordination study of chitosan and Fe³⁺,” *J. Mol. Struct.*, vol.
698 877, no. 1–3, pp. 89–99, Apr. 2008.
- 699 [40] X. Guo *et al.*, “A New Strategy of Lithography Based on Phase Separation of Polymer
700 Blends.,” *Sci. Rep.*, vol. 5, no. Article 15947, Oct. 2015.
- 701 [41] Y. J. Donie *et al.*, “Light trapping in thin film silicon solar cells *via* phase separated
702 disordered nanopillars,” *Nanoscale*, vol. 10, no. 14, pp. 6651–6659, Apr. 2018.
- 703 [42] G. S. Dhillon, S. Kaur, S. K. Brar, and M. Verma, “Green synthesis approach: Extraction
704 of chitosan from fungus mycelia,” *Critical Reviews in Biotechnology*, vol. 33, no. 4. pp.
705 379–403, Dec-2013.
- 706 [43] D. J. M. And and J. J. E. Hardy, “Applications of Functionalized Chitosan in
707 Catalysis†,” *Ind. Eng. Chem. Res.*, vol. 44, no. 23, pp. 8499–8520, 2005.
- 708 [44] P. Van De Witte, P. J. Dijkstra, J. W. A. Van Den Berg, and J. Feijen, “Phase separation
709 processes in polymer solutions in relation to membrane formation,” *ELSEVIER J.*
710 *Membr. Sci.*, vol. 117, pp. 1–31, 1996.
- 711 [45] L. H. Sperling, “Concentrated Solutions, Phase Separation Behavior, and Diffusion,” in

- 712 *Introduction to Physical Polymer Science*, 4th ed., Hoboken, NJ, USA: John Wiley &
713 Sons, Inc., 2005, pp. 145–195.
- 714 [46] M. Vonka and J. Kosek, “Modelling the morphology evolution of polymer materials
715 undergoing phase separation,” *Chem. Eng. J.*, vol. 207, pp. 895–905, 2012.
- 716 [47] M. Voigt *et al.*, “The interplay between the optical and electronic properties of light-
717 emitting-diode applicable conjugated polymer blends and their phase-separated
718 morphology,” *Org. Electron.*, vol. 6, no. 1, pp. 35–45, Feb. 2005.
- 719 [48] O. Aschenbrenner, S. Supasitmongkol, M. Taylor, and P. Styring, “Measurement of
720 vapour pressures of ionic liquids and other low vapour pressure solvents,” *Green Chem.*,
721 vol. 11, no. 8, p. 1217, Aug. 2009.
- 722 [49] A. N. Nesmeyanov and E. V Kikxadze, “Concentration of proteins as a result of the
723 phase separation of water-protein-polysaccharide systems Part 1. Phase equilibria in
724 water-milk proteins-plysaccharide systems,” *Nahrung*, vol. 30, no. 6, pp. 591–599,
725 1986.
- 726 [50] A. N. Nesmeyanov, N. A. Zhuravskaya, E. V Kiknadze, and V. B. Tolstoguzov,
727 “Concentration of proteins as a result of the phase separation of water-protein-
728 polysaccharide systems Part 2. Concentration of milk proteins,” *Nahrung*, vol. 30, no.
729 6, pp. 601–613, 1986.
- 730 [51] Y. Fang, L. Li, C. Inoue, L. Lundin, and I. Appelqvist, “Associative and Segregative
731 Phase Separations of Gelatin/ κ -Carrageenan Aqueous Mixtures,” *Langmuir*, vol. 22, no.
732 23, pp. 9532–9537, Nov. 2006.
- 733 [52] L. M. Dimitrova *et al.*, “Limited coalescence and Ostwald ripening in emulsions
734 stabilized by hydrophobin HFBII and milk proteins,” *Colloids Surfaces A Physicochem.*
735 *Eng. Asp.*, vol. 509, pp. 521–538, Nov. 2016.

- 736 [53] C. Huang, M. Moosmann, J. Jin, T. Heiler, S. Walheim, and T. Schimmel, "Polymer
737 blend lithography: A versatile method to fabricate nanopatterned self-assembled
738 monolayers," *Beilstein J. Nanotechnol.*, vol. 3, pp. 620–628, Sep. 2012.
- 739 [54] M. Sprenger, S. Walheim, A. Budkowski, and U. Steiner, "Hierarchic Structure
740 Formation in Binary and Ternary Polymer Blends," *Interface Sci.*, vol. 11, no. 2, pp.
741 225–235, 2003.
- 742 [55] L. Cui, H. Wang, Y. Ding, and Y. Han, "Tunable ordered droplets induced by convection
743 in phase-separating P2VP/PS blend film," *Polymer (Guildf.)*, vol. 45, no. 24, pp. 8139–
744 8146, Nov. 2004.
- 745 [56] L. Xue, J. Zhang, and Y. Han, "Phase separation induced ordered patterns in thin
746 polymer blend films," *Prog. Polym. Sci.*, vol. 37, no. 4, pp. 564–594, Apr. 2012.
- 747 [57] C. Huang, A. Förste, S. Walheim, and T. Schimmel, "Polymer blend lithography for
748 metal films: large-area patterning with over 1 billion holes/inch ²," *Beilstein J.*
749 *Nanotechnol.*, vol. 6, pp. 1205–1211, May 2015.
- 750 [58] G. Filippone, P. A. Netti, and D. Acierno, "Microstructural evolutions of LDPE/PA6
751 blends by rheological and rheo-optical analyses: Influence of flow and compatibilizer
752 on break-up and coalescence processes," *Polymer (Guildf.)*, vol. 48, no. 2, pp. 564–573,
753 2007.
- 754 [59] J. Jůza and I. Fortelný, "Flow-Induced Coalescence: Evaluation of Some
755 Approximations," *Macromol. Symp.*, vol. 373, no. 1, pp. 1–10, Jun. 2017.
- 756 [60] I. Fortelný, J. Jůza, and B. Dimzoski, "Coalescence in quiescent polymer blends with a
757 high content of the dispersed phase," *Eur. Polym. J.*, vol. 48, no. 7, pp. 1230–1240, Jul.
758 2012.
- 759 [61] S. Roy and A. Sharma, "Self-organized morphological evolution and dewetting in

- 760 solvent vapor annealing of spin coated polymer blend nanostructures,” *J. Colloid*
761 *Interface Sci.*, vol. 449, pp. 215–225, Jul. 2015.
- 762 [62] K. Ji-Seon, P. K. H. Ho, C. E. Murphy, and R. H. Friend, “Phase Separation in
763 Polyfluorene-Based Conjugated Polymer Blends: Lateral and Vertical Analysis of Blend
764 Spin-Cast Thin Films,” *Macromolecules*, vol. 37, no. 8, pp. 2861–2871, 2004.
- 765 [63] T. Ghoshal *et al.*, “Size and space controlled hexagonal arrays of superparamagnetic
766 iron oxide nanodots: magnetic studies and application,” *Sci. Rep.*, vol. 3, no. 1, p. Article
767 No. 2772, Dec. 2013.
- 768 [64] E. Guibal, T. Vincent, and R. Navarro, “Metal ion biosorption on chitosan for the
769 synthesis of advanced materials,” *J. Mater. Sci.*, vol. 49, no. 16, pp. 5505–5518, Aug.
770 2014.
- 771 [65] V. Mohanasrinivasan *et al.*, “Studies on heavy metal removal efficiency and
772 antibacterial activity of chitosan prepared from shrimp shell waste.,” *3 Biotech*, vol. 4,
773 no. 2, pp. 167–175, Apr. 2014.
- 774 [66] A. . Varma, S. . Deshpande, and J. . Kennedy, “Metal complexation by chitosan and its
775 derivatives: a review,” *Carbohydr. Polym.*, vol. 55, no. 1, pp. 77–93, Jan. 2004.
- 776 [67] E. Guibal, “Interactions of metal ions with chitosan-based sorbents: a review,” *Sep.*
777 *Purif. Technol.*, vol. 38, no. 1, pp. 43–74, Jul. 2004.
- 778 [68] N. Horzum, E. Boyacı, A. E. Eroğlu, T. Shahwan, and M. M. Demir, “Sorption
779 Efficiency of Chitosan Nanofibers toward Metal Ions at Low Concentrations,”
780 *Biomacromolecules*, vol. 11, no. 12, pp. 3301–3308, Dec. 2010.
- 781 [69] H. I. Okur *et al.*, “Beyond the Hofmeister Series: Ion-Specific Effects on Proteins and
782 Their Biological Functions,” *J. Phys. Chem. B*, vol. 121, no. 9, pp. 1997–2014, Mar.
783 2017.

- 784 [70] M. K. Braun *et al.*, “Reentrant Phase Behavior in Protein Solutions Induced by
785 Multivalent Salts: Strong Effect of Anions Cl⁻ – Versus NO₃⁻,” *J. Phys. Chem. B*, vol.
786 122, no. 50, pp. 11978–11985, Dec. 2018.
- 787 [71] R. Senthil Kumar and P. Rajkumar, “Characterization of minerals in air dust particles in
788 the state of Tamilnadu, India through FTIR, XRD and SEM analyses,” *Infrared Phys.*
789 *Technol.*, vol. 67, pp. 30–41, Nov. 2014.
- 790 [72] T. F. Young, C. P. Chen, J. F. Liou, Y. L. Yang, and T. C. Chang, “Study on the Si–Si
791 Vibrational States of the Near Surface Region of Porous Silicon,” *J. Porous Mater.*, vol.
792 7, no. 1/3, pp. 339–343, 2000.
- 793 [73] M. A. Girsova, G. F. Golovina, I. N. Anfimova, M. Y. Arsent’ev, and T. V Antropova,
794 “Structure and spectral properties of the silver-containing high-silica glasses,” *J. Phys.*
795 *Conf. Ser.*, vol. 741, no. 1, pp. 1–5, Aug. 2016.
- 796 [74] P. Garidel and H. Schott, “Fourier-Transform Midinfrared Spectroscopy for Analysis
797 and Screening of Liquid Protein Formulations, Part 1,” *BioProcess Tech.*, vol. 4, no. 5,
798 pp. 40–46, 2006.
- 799 [75] J. R. Smith, M. T. Cicerone, and C. W. Meuse, “Tertiary Structure Changes in Albumin
800 upon Surface Adsorption Observed via Fourier Transform Infrared Spectroscopy,”
801 *Langmuir*, vol. 25, no. 8, pp. 4571–4578, Apr. 2009.
- 802 [76] P. Murugaraj, D. E. Mainwaring, D. C. Tonkin, and M. Al Kobaisi, “Probing the
803 dynamics of water in chitosan polymer films by dielectric spectroscopy,” *J. Appl. Polym.*
804 *Sci.*, vol. 120, no. 3, pp. 1307–1315, May 2011.
- 805 [77] L. Guo, G. Liu, R.-Y. Hong, and H.-Z. Li, “Preparation and Characterization of Chitosan
806 Poly(acrylic acid) Magnetic Microspheres,” *Mar. Drugs*, vol. 8, no. 7, pp. 2212–2222,
807 Jul. 2010.

- 808 [78] P. Monvisade and P. Siriphannon, "Chitosan intercalated montmorillonite: Preparation,
809 characterization and cationic dye adsorption," *Appl. Clay Sci.*, vol. 42, no. 3–4, pp. 427–
810 431, Jan. 2009.
- 811 [79] M. M. A. Al-Remawi, "Properties of Chitosan Nanoparticles Formed Using Sulfate
812 Anions as Crosslinking Bridges," *Am. J. Appl. Sci.*, vol. 9, no. 7, pp. 1091–1100, 2012.
- 813 [80] S. Kunjachan, S. Gupta, A. K. Dwivedi, A. Dube, and M. K. Chourasia, "Chitosan-based
814 macrophage-mediated drug targeting for the treatment of experimental visceral
815 leishmaniasis," *J. Microencapsul.*, vol. 28, no. 4, pp. 301–310, Jun. 2011.
- 816 [81] T.-C. Yang and K. C. Saraswat, "Effect of Physical Stress on the Degradation of Thin
817 SiO₂ Films Under Electrical Stress," *IEEE Trans. Electron Devices*, vol. 47, no. 4, pp.
818 746–755, 2000.
- 819 [82] F. Matteini, G. Tütüncüoğlu, D. Ruffer, E. Alarcón-Lladó, and A. Fontcuberta i Morral,
820 "Ga-assisted growth of GaAs nanowires on silicon, comparison of surface SiO_x of
821 different nature," *J. Cryst. Growth*, vol. 404, pp. 246–255, Oct. 2014.
- 822 [83] T. Ghoshal *et al.*, "Fabrication of ultra-dense sub-10 nm in-plane Si nanowire arrays by
823 using a novel block copolymer method: optical properties.," *Nanoscale*, vol. 8, no. 4,
824 pp. 2177–87, Jan. 2016.
- 825 [84] R. Prakash, R. J. Choudhary, L. S. S. Chandra, N. Lakshmi, and D. M. Phase, "Electrical
826 and magnetic transport properties of Fe₃O₄ thin films on GaAs (100) substrate," *J. Phys.*
827 *Condens. Matter*, vol. 19, no. 48, p. 486212, Dec. 2009.
- 828 [85] C.-Y. Shih *et al.*, "Two mechanisms of nanoparticle generation in picosecond laser
829 ablation in liquids: the origin of the bimodal size distribution," *Nanoscale*, vol. 10, no.
830 15, pp. 6900–6910, Apr. 2018.
- 831 [86] I. Prieto *et al.*, "Bi-modal nanoheteroepitaxy of GaAs on Si by metal organic vapor phase

- 832 epitaxy,” *Nanotechnology*, vol. 28, no. 13, p. 135701, Mar. 2017.
- 833 [87] T. T. Morgan, T. M. Goff, and J. H. Adair, “The colloidal stability of fluorescent calcium
834 phosphosilicate nanoparticles: the effects of evaporation and redispersion on particle
835 size distribution,” *Nanoscale*, vol. 3, no. 5, pp. 2044–2053, May 2011.
- 836 [88] J. Wallecan, C. McCrae, S. J. J. Debon, J. Dong, and J. Mazoyer, “Emulsifying and
837 stabilizing properties of functionalized orange pulp fibers,” *Food Hydrocoll.*, vol. 47,
838 pp. 115–123, May 2015.
- 839 [89] W. N. Ha, F. Shakibaie, B. Kahler, and L. J. Walsh, “Deconvolution of the particle size
840 distribution of ProRoot MTA and MTA Angelus.,” *Acta Biomater. Odontol. Scand.*, vol.
841 2, no. 1, pp. 7–11, Jan. 2016.
- 842 [90] V. E. Ziegler and B. A. Wolf, “Bimodal drop size distributions during the early stages
843 of shear induced coalescence,” *Polymer (Guildf.)*, vol. 46, no. 22, pp. 9265–9273, Oct.
844 2005.
- 845 [91] A. Rezaei Kolahchi, P. J. Carreau, and A. Ajji, “Surface Roughening of PET Films
846 through Blend Phase Coarsening,” *ACS Appl. Mater. Interfaces*, vol. 6, no. 9, pp. 6415–
847 6424, May 2014.
- 848 [92] A. B. Reddy, G. S. M. Reddy, V. Sivanjineyulu, J. Jayaramudu, K. Varaprasad, and E.
849 R. Sadiku, *Design and Applications of Nanostructured Polymer Blends and*
850 *Nanocomposite Systems*, 1st ed. Elsevier Inc., 2016.
- 851 [93] F. Jara, O. E. Pérez, and A. M. R. Pilosof, “Impact of phase separation of whey
852 proteins/hydroxypropylmethylcellulose mixtures on gelation dynamics and gels
853 properties,” *Food Hydrocoll.*, vol. 24, no. 6–7, pp. 641–651, Aug. 2010.
- 854 [94] N. Kimura, K. Kawazoe, H. Nakanishi, T. Norisuye, and Q. Tran-Cong-Miyata,
855 “Influences of wetting and shrinkage on the phase separation process of polymer

856 mixtures induced by photopolymerization,” *Soft Matter*, vol. 9, no. 35, p. 8428, 2013.

857 [95] T. Geldhauser, S. Walheim, T. Schimmel, P. Leiderer, and J. Boneberg, “Influence of

858 the relative humidity on the demixing of polymer blends on prepatterned substrates,”

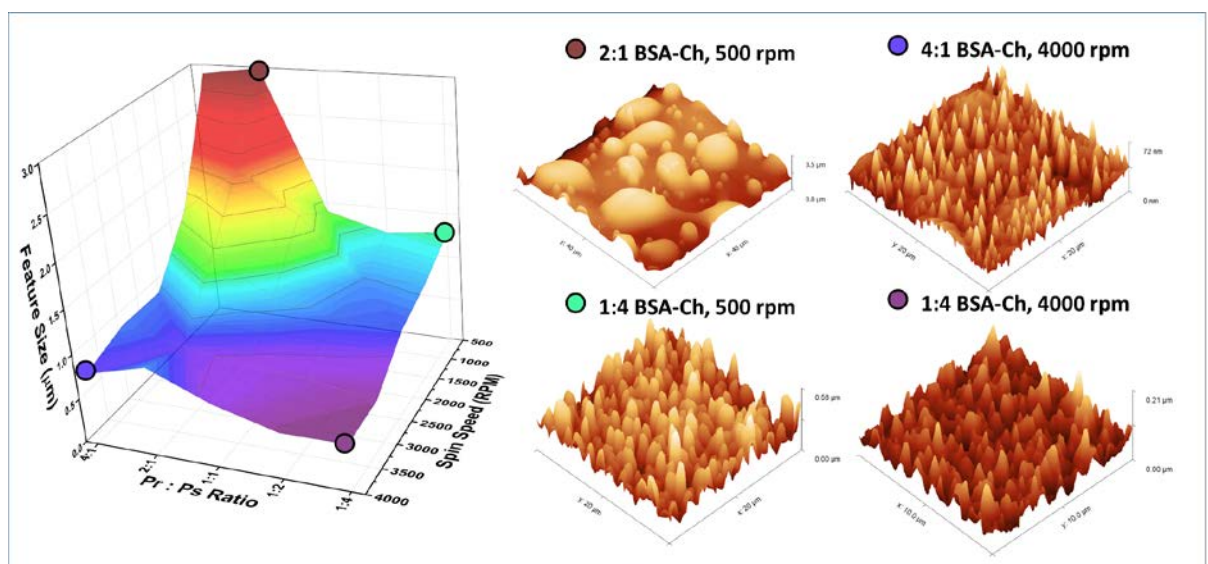
859 *Macromolecules*, vol. 43, no. 2, pp. 1124–1128, Jan. 2010.

860 [96] H. Zhang and F. Wang, “Analysis of surface wettability of synthetic magnetite,” *J.*

861 *Wuhan Univ. Technol. Mater. Sci. Ed.*, vol. 29, no. 4, pp. 679–683, 2014.

862

863 **Graphical Abstract**



864

865

866

867

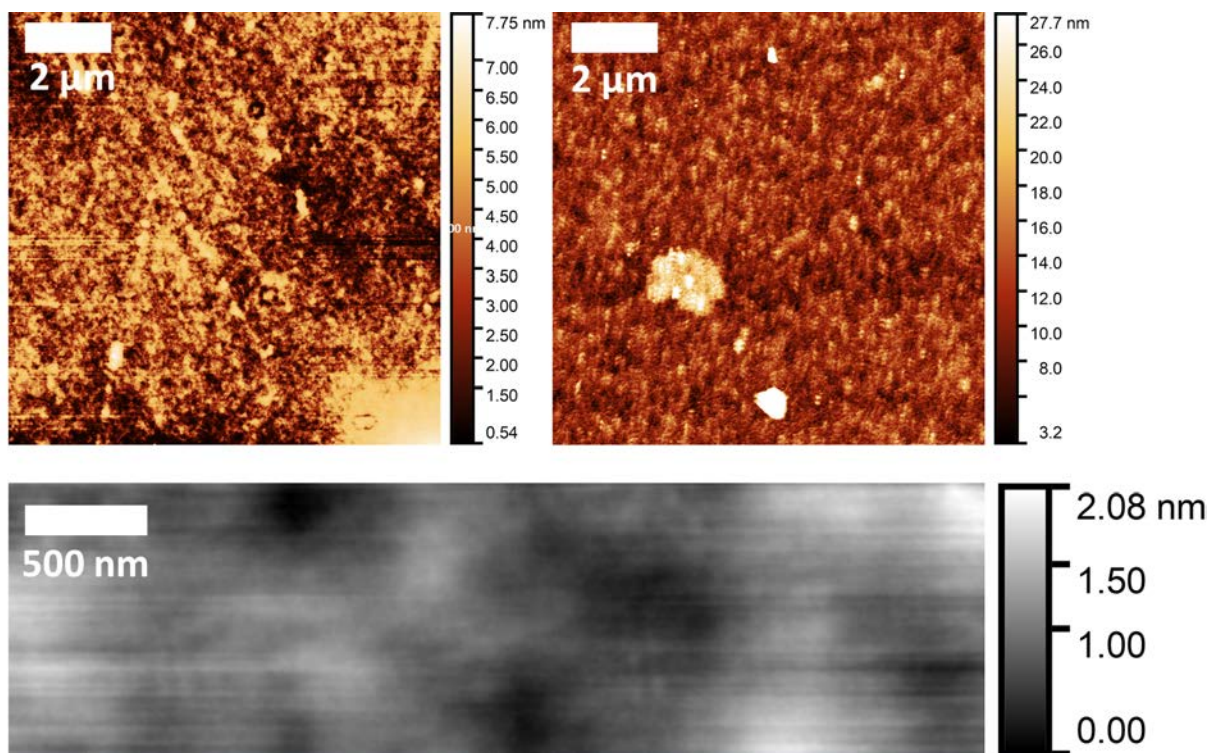
868

869

870 **Supporting Information**

871 **Solution Preparation**

872 Prior to dissolution, proteins, and polysaccharides were dried overnight at room temperature
873 under vacuum. Biopolymer stock solutions were made by solubilising Ch and BSA in 90 %
874 FA at 5 w/v%, 10 w/v%. These solutions were stirred in a closed vessel for 3 h at room
875 temperature. The solutions were then centrifuged at 13,000 rpm in a Beckman Coulter Avanti
876 J-26XPI centrifuge at 18 °C for 15 min and decanted. Following this, stock solutions were
877 stored at -20 °C for further use or used immediately. Stock solutions were diluted with fresh
878 FA and/or mixed with each other to produce coating solutions.



879
880 **Figure S1:** AFM images showing results of casting neat thin-films at 65 % relative
881 humidity at 2000 rpm prepared in the same manner as BSA-Ch blends. Biopolymer AFM
882 images are red, glass substrate AFM image is grey. Shows 1% BSA film (left), 1% chitosan
883 film (right) and glass substrate (bottom). Scale bars top left hand corner of each image.

884

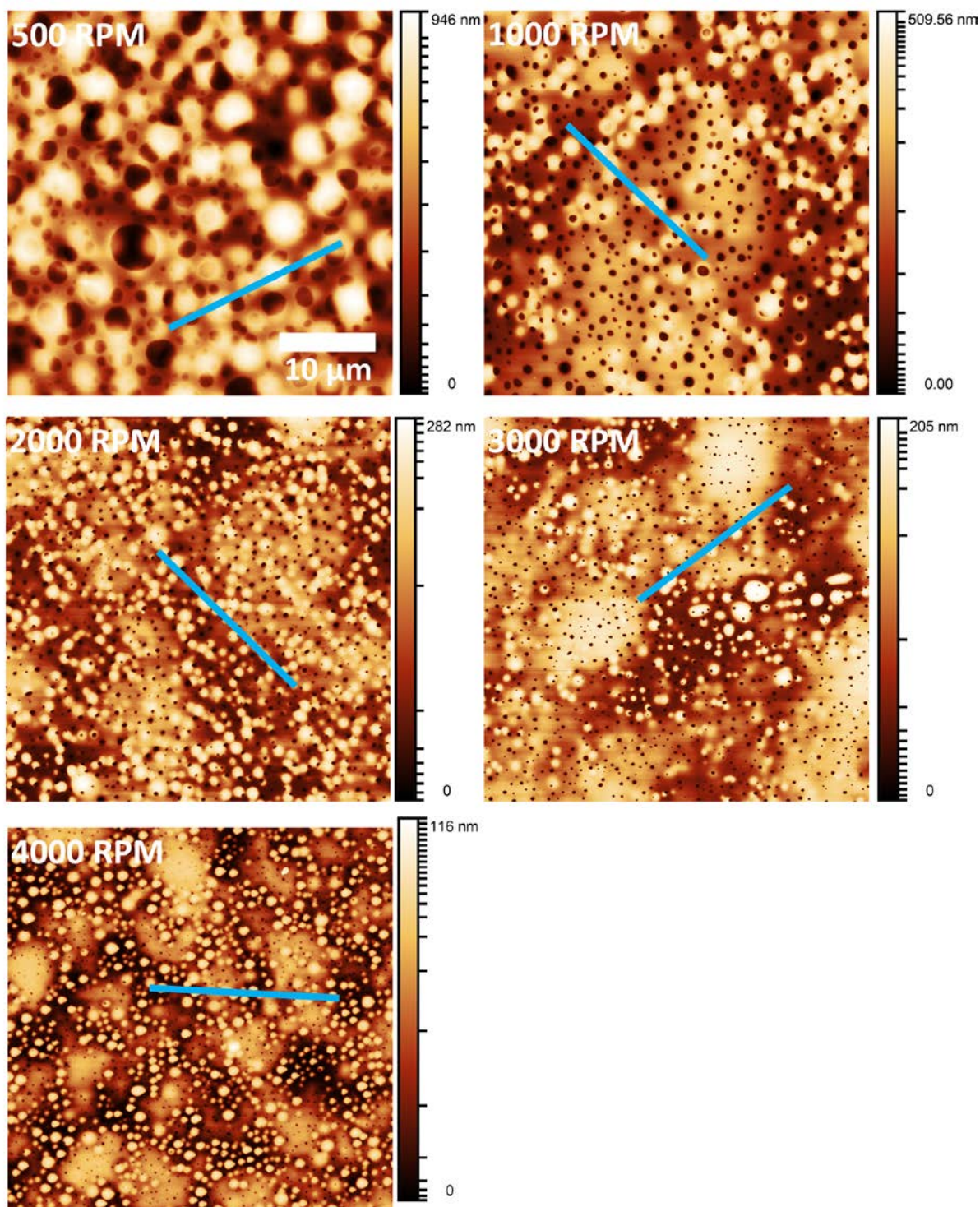
885

886

887

888

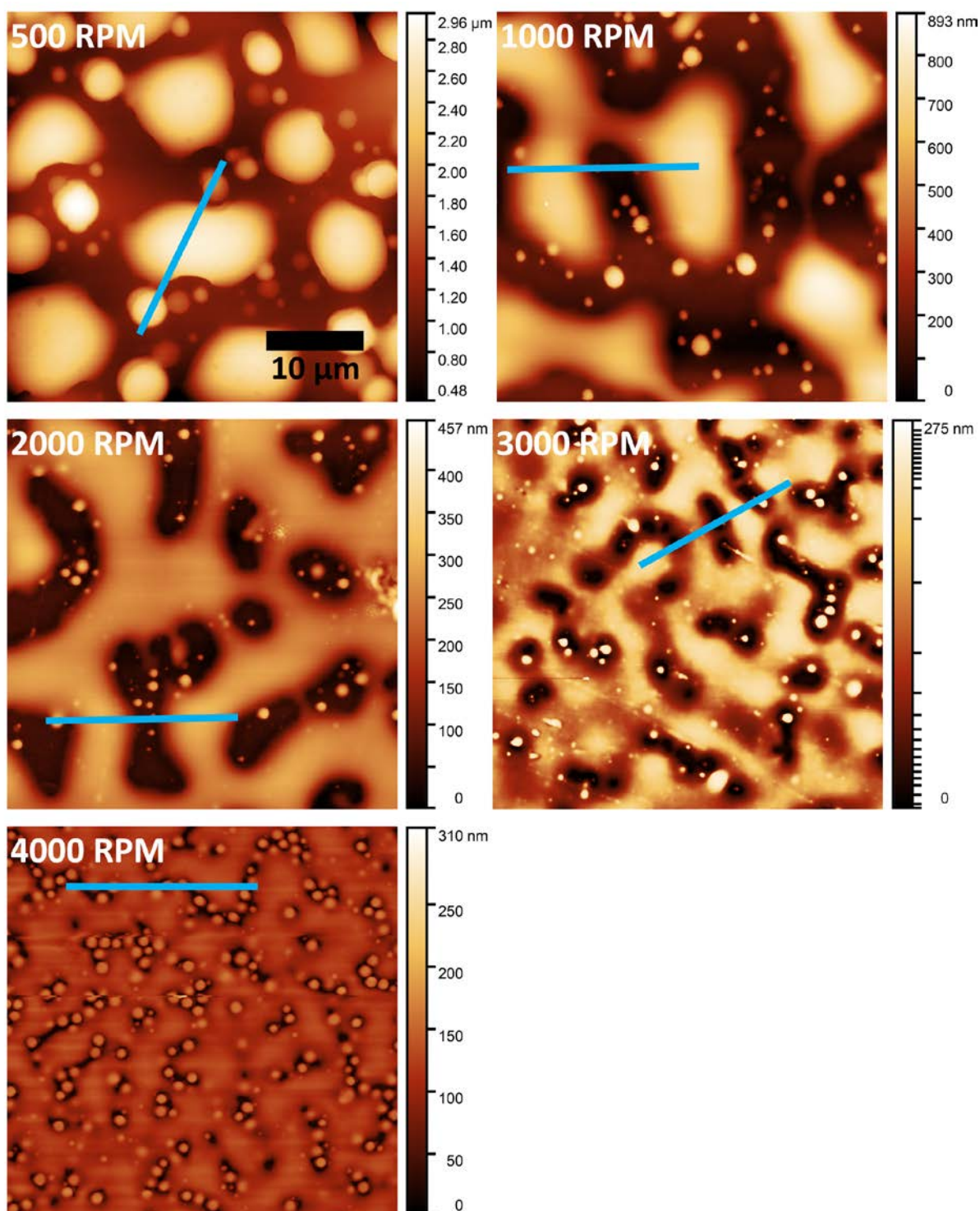
889



890

891 **Figure S2:** AFM images depicting the effect spin speed in ambient air (65 % RH) for the
 892 4:1 BSA-Ch blend. Each image is $40\ \mu\text{m} \times 40\ \mu\text{m}$ area (scale bar $10\ \mu\text{m}$, shown in the 500
 893 rpm image). Line profile denoted by blue line.

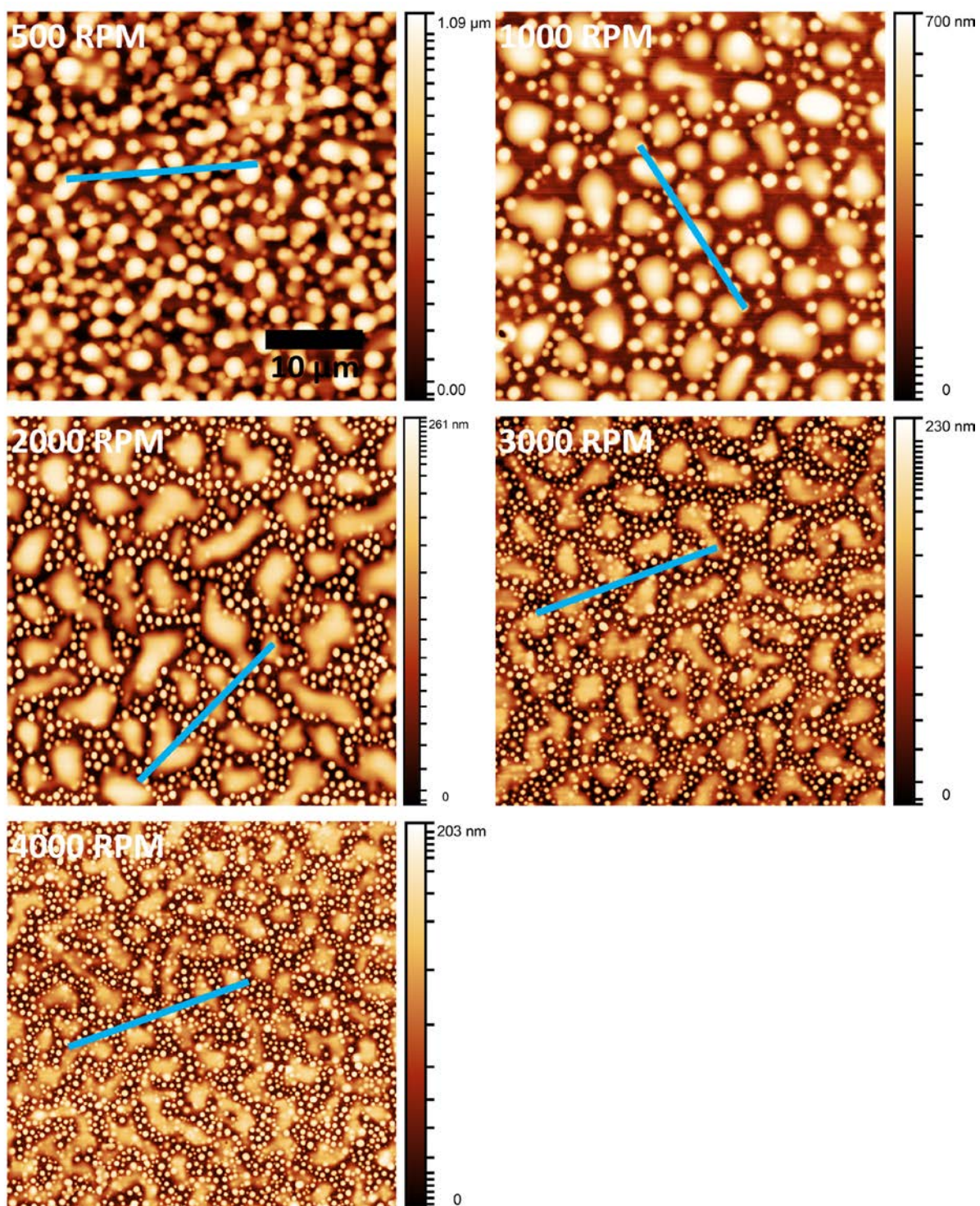
894



895

896 *Figure S3: AFM images depicting the effect spin speed in ambient air (65 % RH) for the*
 897 *4:1 BSA-Ch blend. Each image is 40 μm × 40 μm area (scale bar 10 μm, shown in the 500*
 898 *rpm image). Line profile denoted by blue line.*

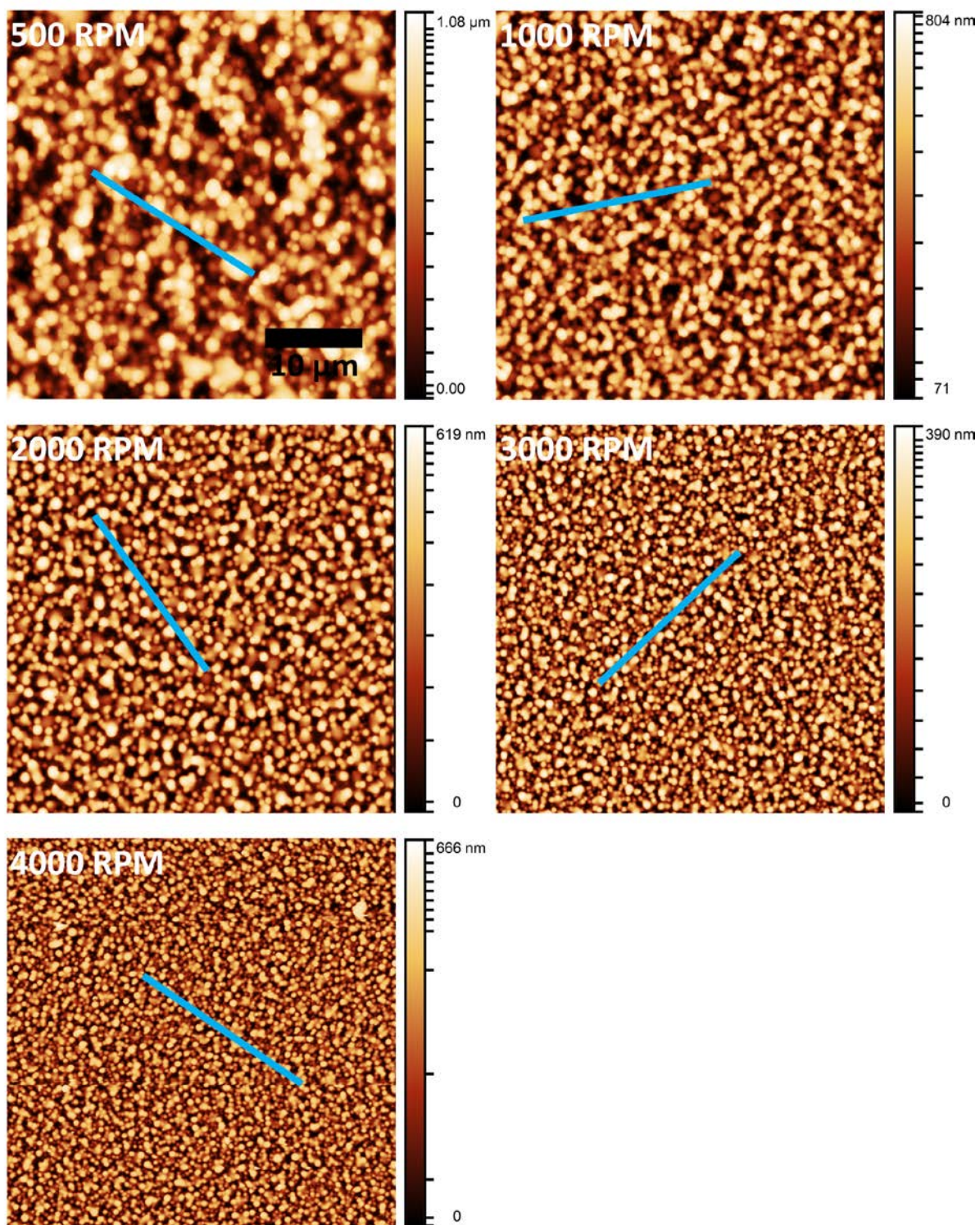
899



900

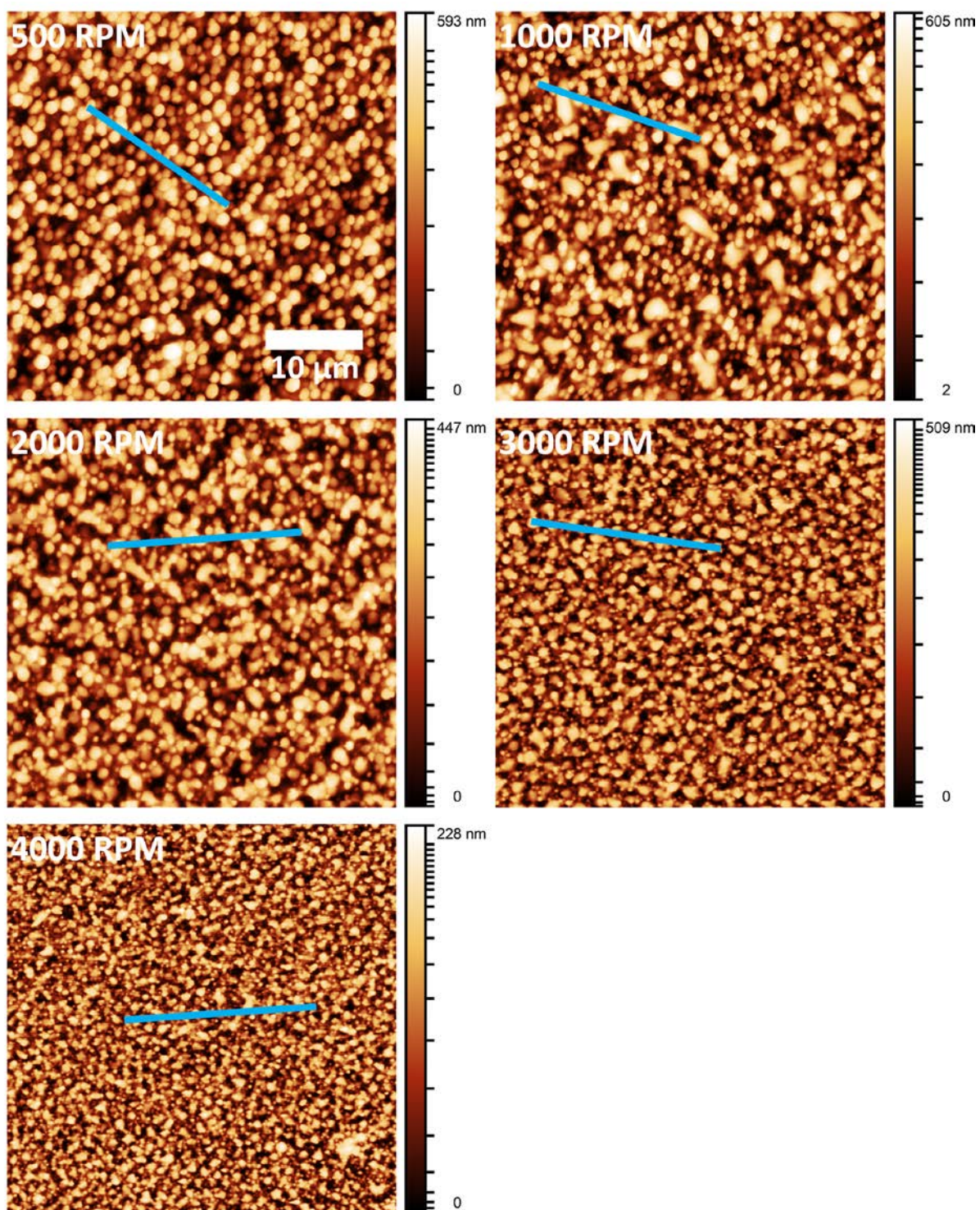
901 **Figure S4:** AFM images depicting the effect spin speed in ambient air (65 % RH) for the
 902 1:1 BSA-Ch blend. Each image is $40\ \mu\text{m} \times 40\ \mu\text{m}$ area (scale bar $10\ \mu\text{m}$, shown in the 500
 903 rpm image). Line profile denoted by blue line.

904



905

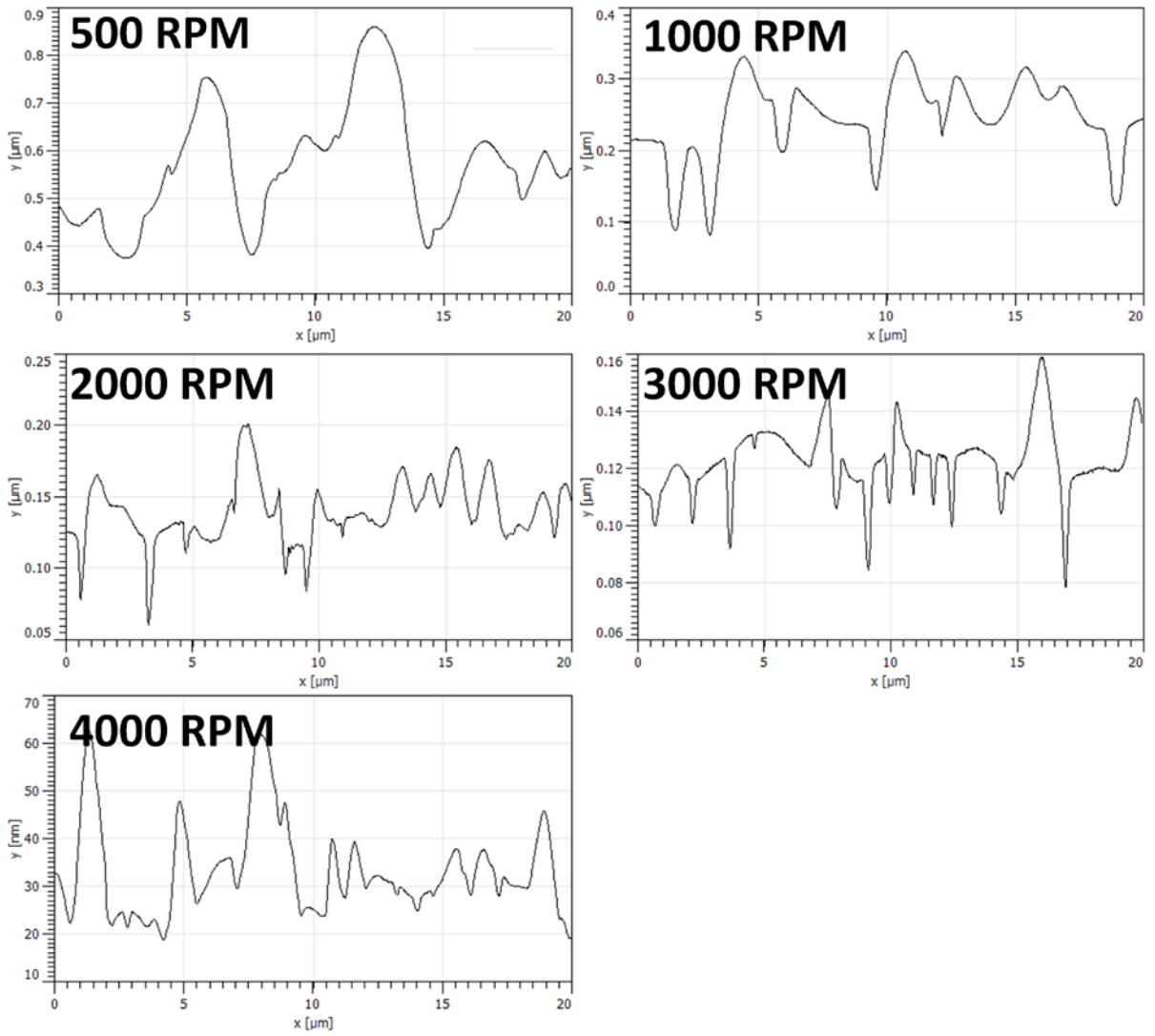
906 *Figure S5: AFM images depicting the effect spin speed in ambient air (65 % RH) for the*
 907 *1:2 BSA-Ch blend. Each image is 40 μm × 40 μm area (scale bar 10 μm, shown in the 500*
 908 *rpm image). Line profile denoted by blue line.*



910

911 **Figure S6:** AFM images depicting the effect spin speed in ambient air (65 % RH) for the
 912 1:2 BSA-Ch blend. Each image is $40\ \mu\text{m} \times 40\ \mu\text{m}$ area (scale bar $10\ \mu\text{m}$, shown in the 500
 913 rpm image). Line profile denoted by blue line.

4% : 1%



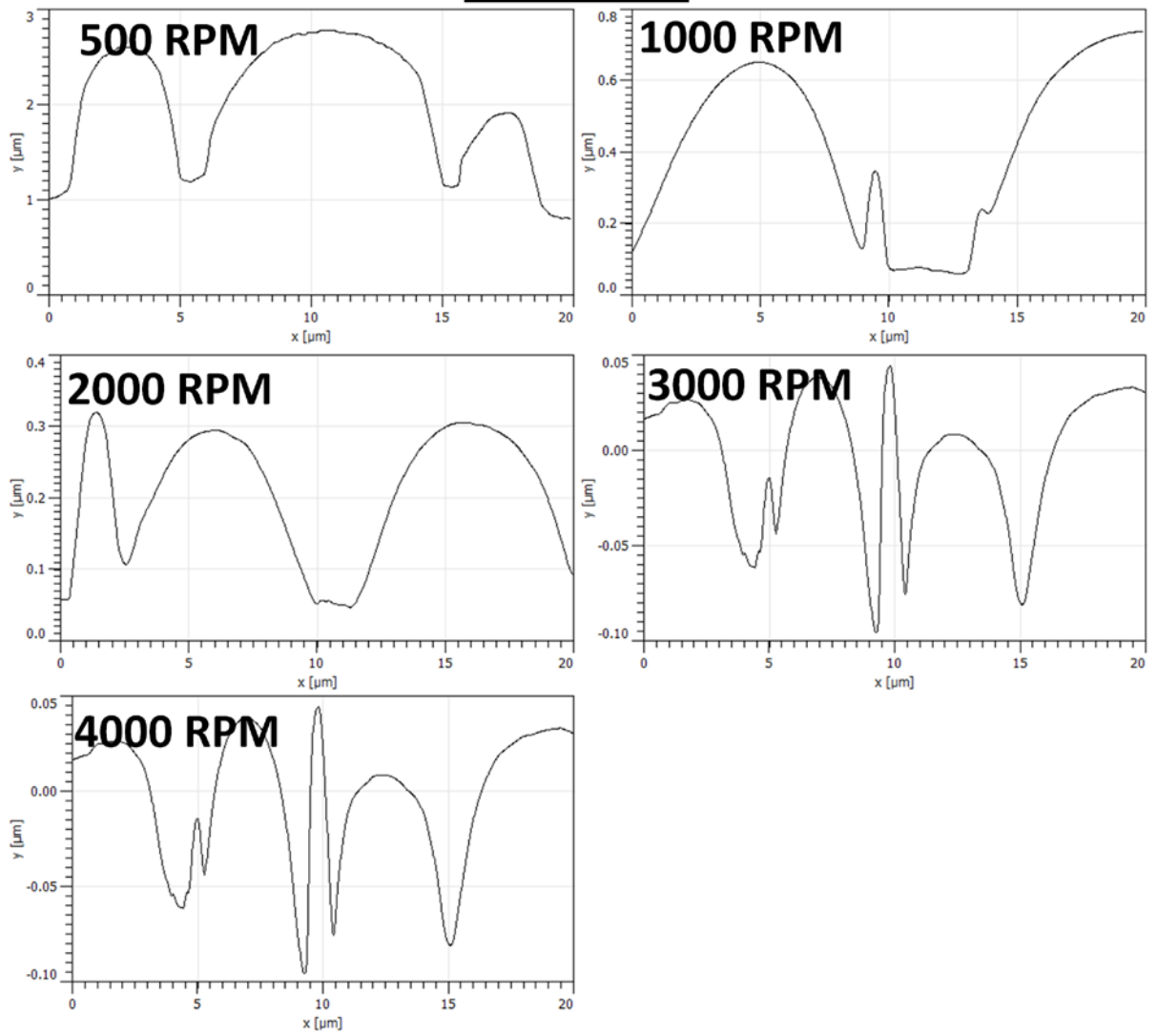
915

916

Figure S7: 20 μm line profiles for all 4:1 BSA-Ch.

917

2% : 1%



918

919 *Figure S8: 20 μm line profiles for all 2:1 BSA-Ch.*

920

921

922

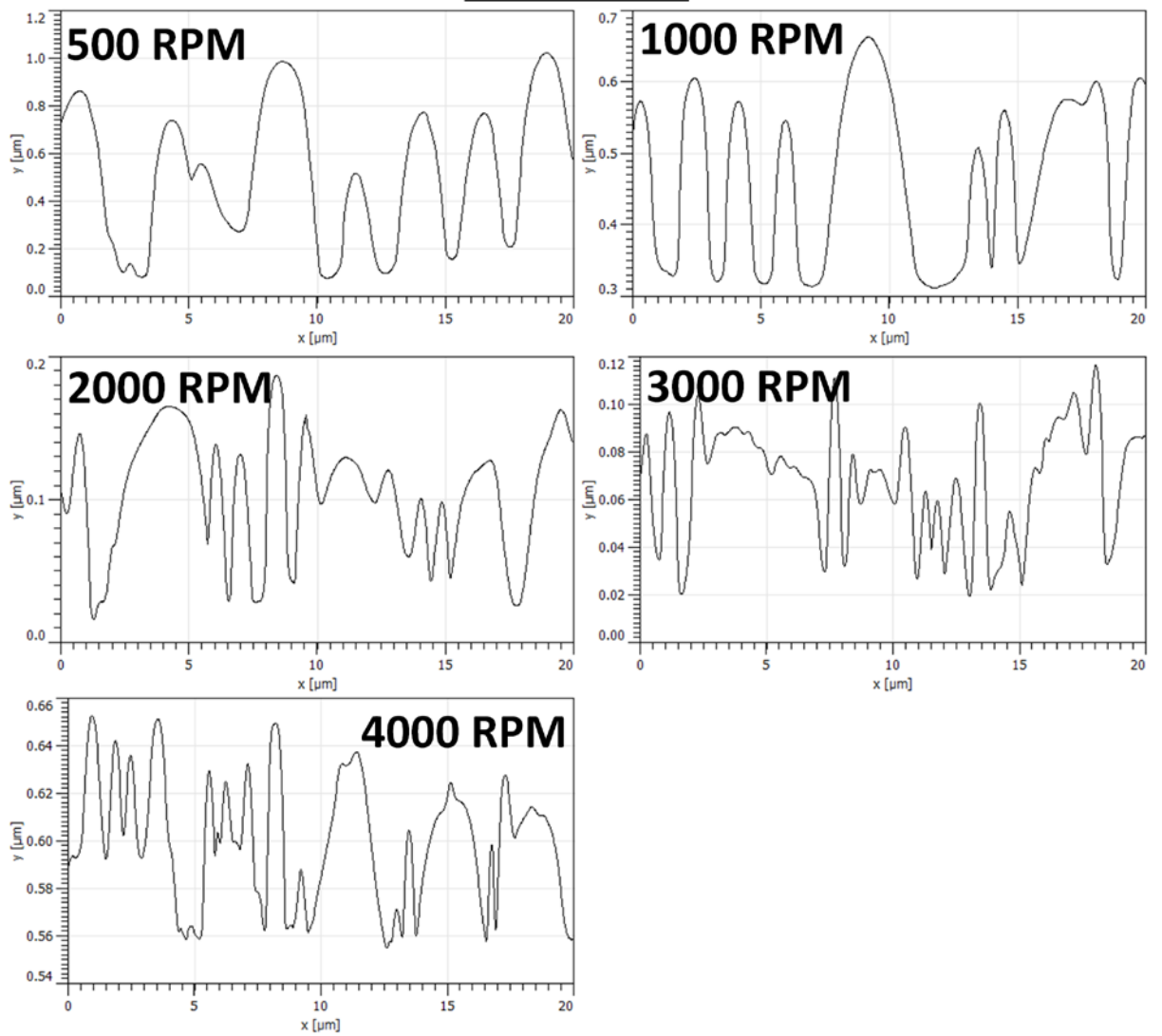
923

924

925

926

1% : 1%



927

928

Figure S9: 20 μm line profiles for all 1:1 BSA-Ch.

929

930

931

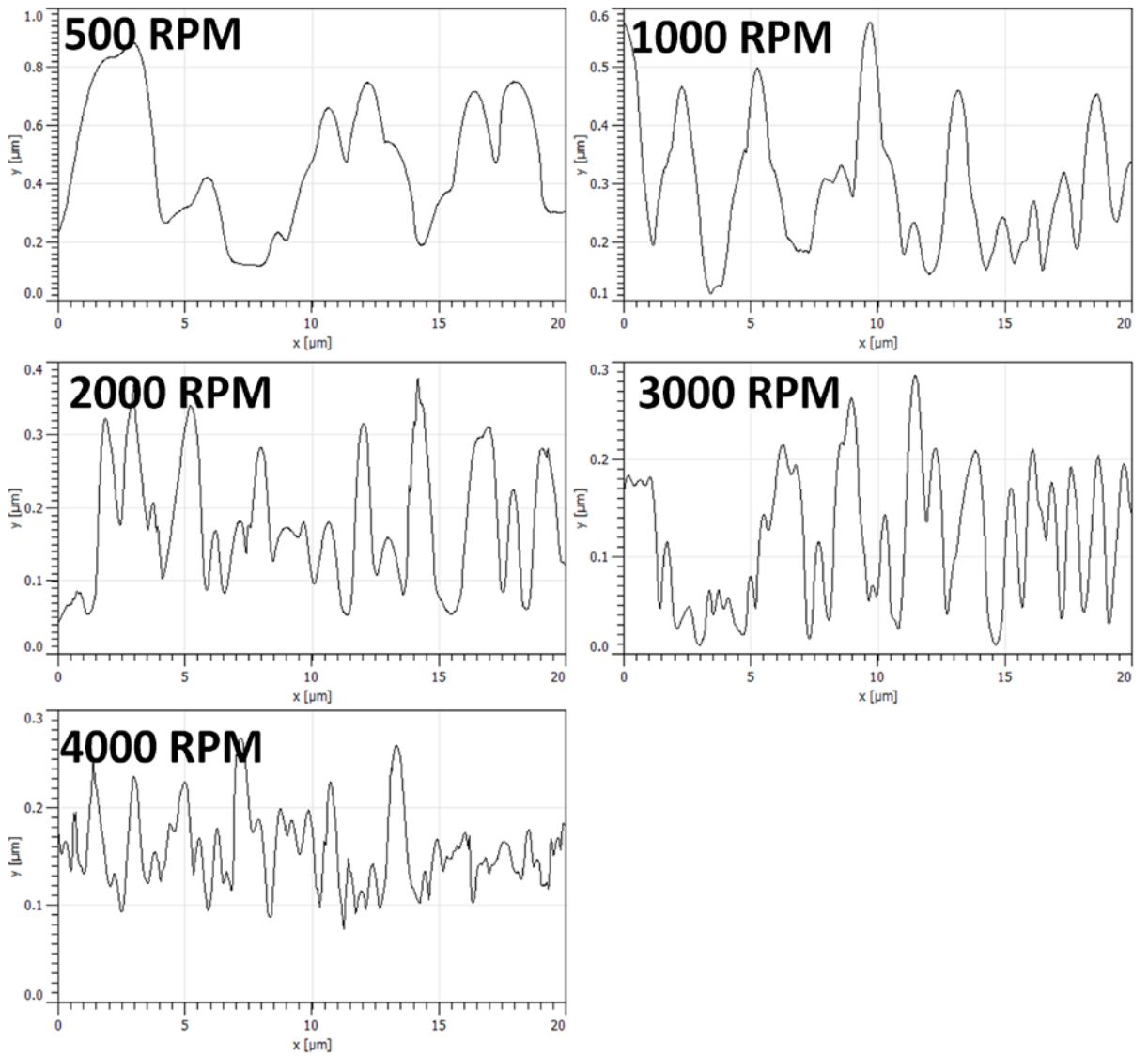
932

933

934

935

1% : 2%



936

937 *Figure S10: 20 μm line profiles for all 1:2 BSA-Ch.*

938

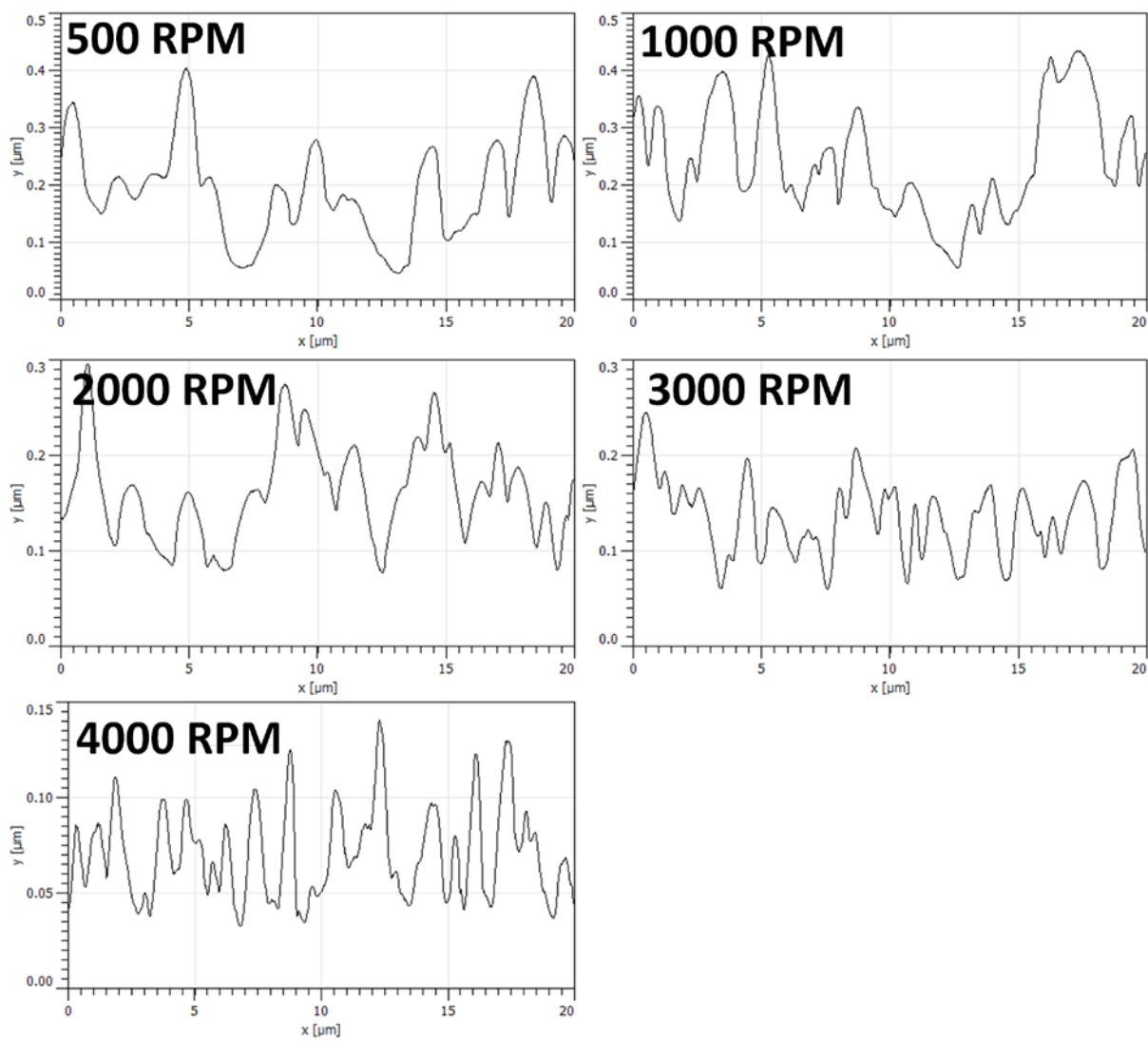
939

940

941

942

943

1% : 4%

945

946 ***Figure S11: 20 μm line profiles for all 1:4 BSA-Ch.***

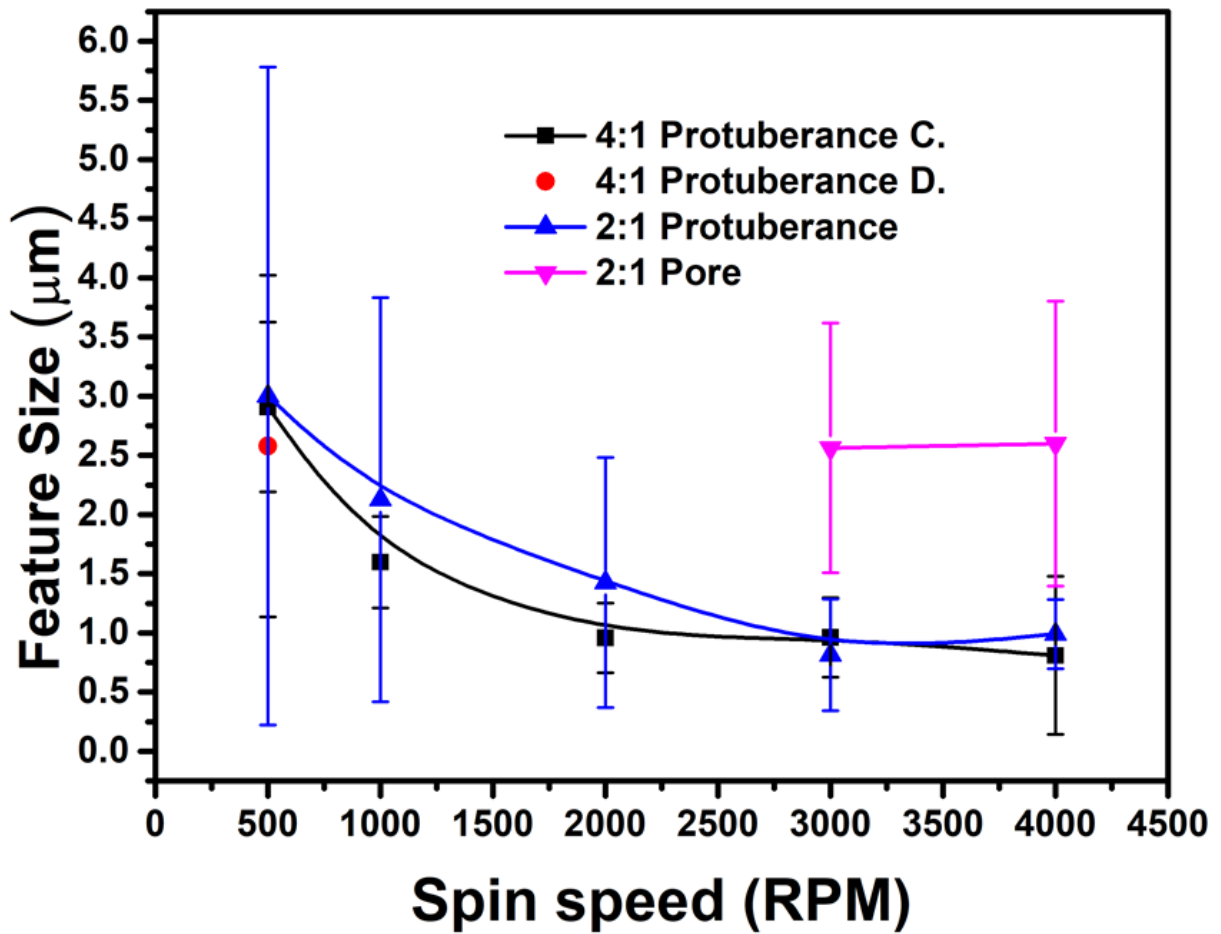
947

948

949

950

951



952

953 *Figure S12:* Statistical analysis of BSA-Ch blends feature diameter plotted against spin speed.

954 All but the 2:1 blend refers to protuberance measurements, with the 2:1 blend data displaying

955 both protuberance and pore data separately. The circular legend for the 4:1 blend refers to

956 feature diameter in the discontinuous domain, i.e. salami structure regions.

957

958

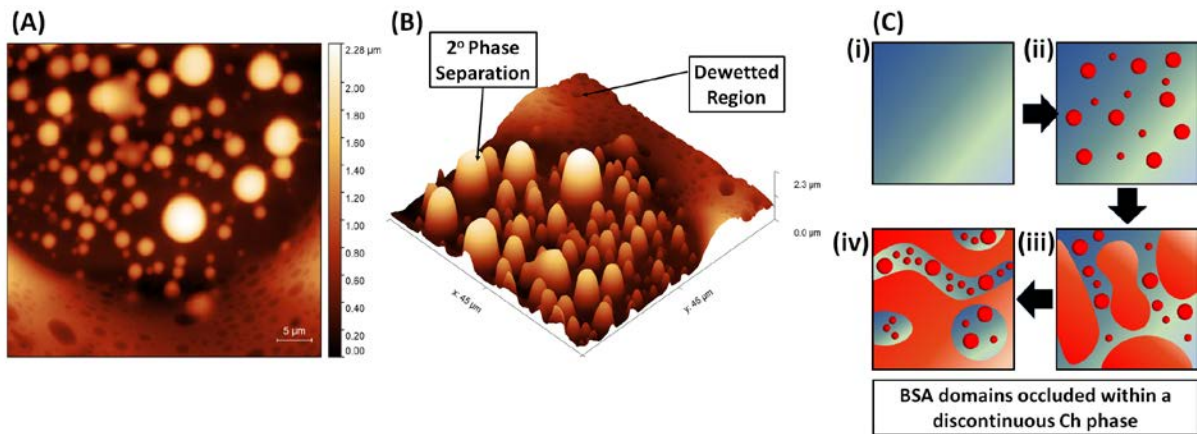
959

960

961

962

963



964

965

966

967

968

969

970

971

972

973

974

975

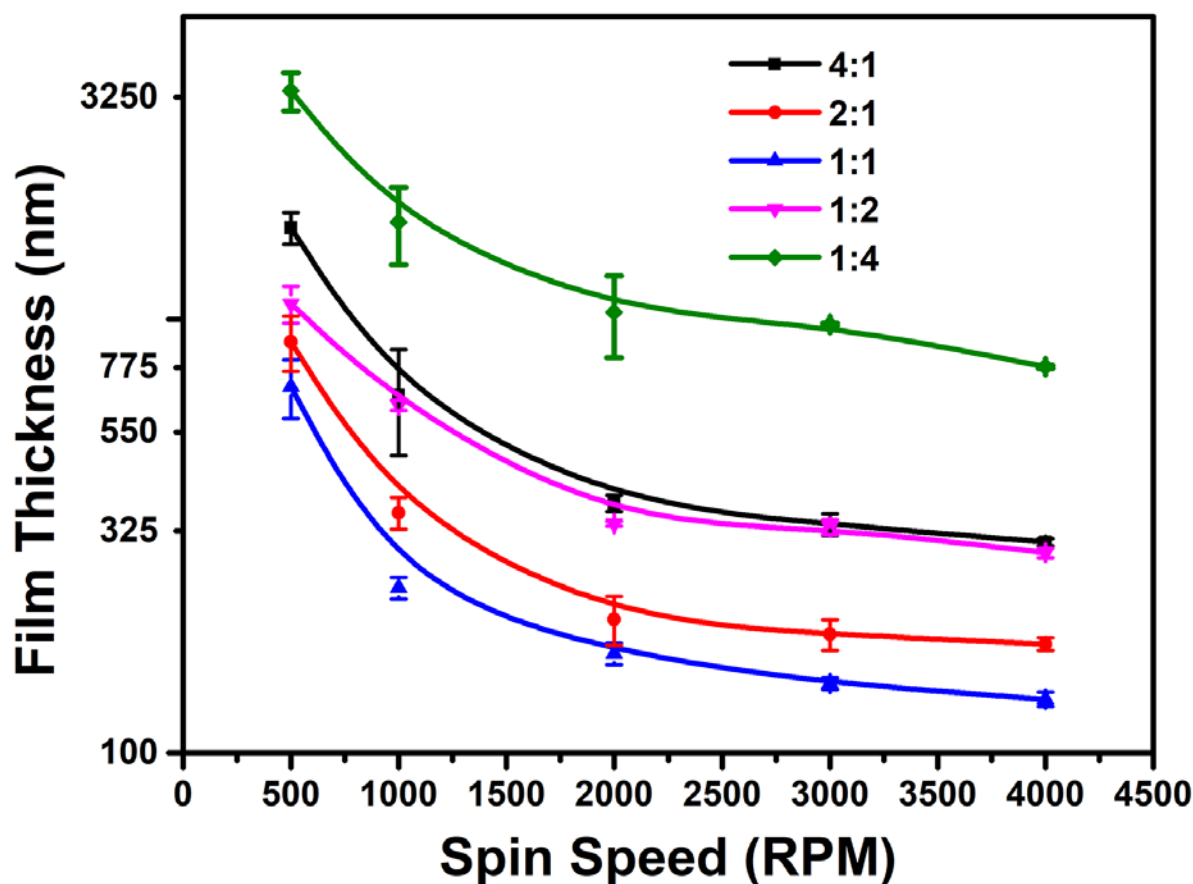
976

977

978

979

Figure S13: *A and B*) 2D and 3D AFM images of 4:1 BSA-Ch blend salami structures, inset scale bar 5 μm. *C*) Mechanism of occlusion of the discontinuous phase. **Figure S7C** (i) shows homogenous solution before phase separation, (ii) shows blend phase separation, (iii) shows elongated structures which may result from coalescence or high shear forces and (iv) phase occlusion and adoption of salami structure.



981

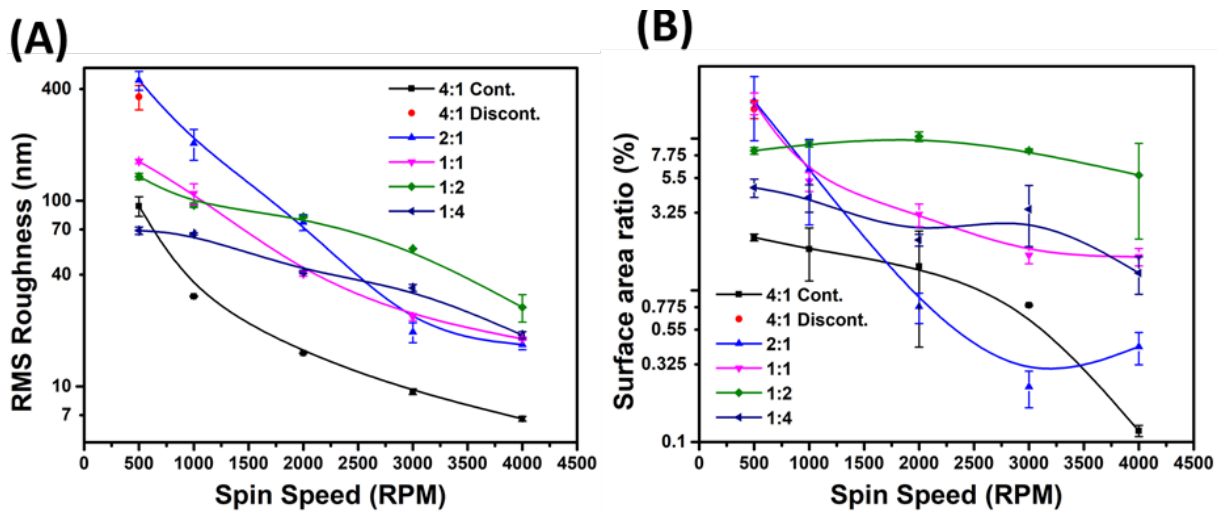
982 *Figure S14:* Plots the average film thickness (nm) vs spin speed (rpm) for all BSA-Ch
 983 blends.

984

985 *Figure S14* shows the average film thickness of BSA-Ch blends. 1:1 BSA-Ch films are
 986 the thinnest, due to low solution viscosity. Doubling the BSA wt % in the 2:1 BSA-Ch blends
 987 increases film thickness due to increased solution viscosity. As Ch produces more viscous
 988 solutions in formic acid, the 1:2 BSA-Ch blend produces thicker films than the 1:1 or 2:1 BSA-
 989 Ch blends. Similarly, the 4:1 BSA-Ch blend is thicker than the 2:1 BSA-Ch blend. However,
 990 at higher spin speeds (≥ 2000 rpm) 1:2 BSA-Ch blends have equivalent film thickness
 991 measurements to 4:1 BSA-Ch blends. This is most likely due to faster evaporation during spin

992 coating resulting in more viscous solutions. This, in turn, would result in more Ch retained on
 993 the substrate. As the most viscous solution, the 1:4 BSA-Ch films are the thickest. All blends
 994 (with the exception of the 1:4 BSA-Ch blend) achieved minimal reduction in film thickness
 995 with speeds exceeding 2000 rpm. The 4:1 BSA-Ch blend was the only blend to result in salami
 996 structure formation.

997



998

999 *Figure S15: A) Plots the RMS roughness vs spin speed for all BSA-Ch blends. B) Plots*
 1000 *the surface area ratio (%) vs spin speed for all BSA-Ch blends.*

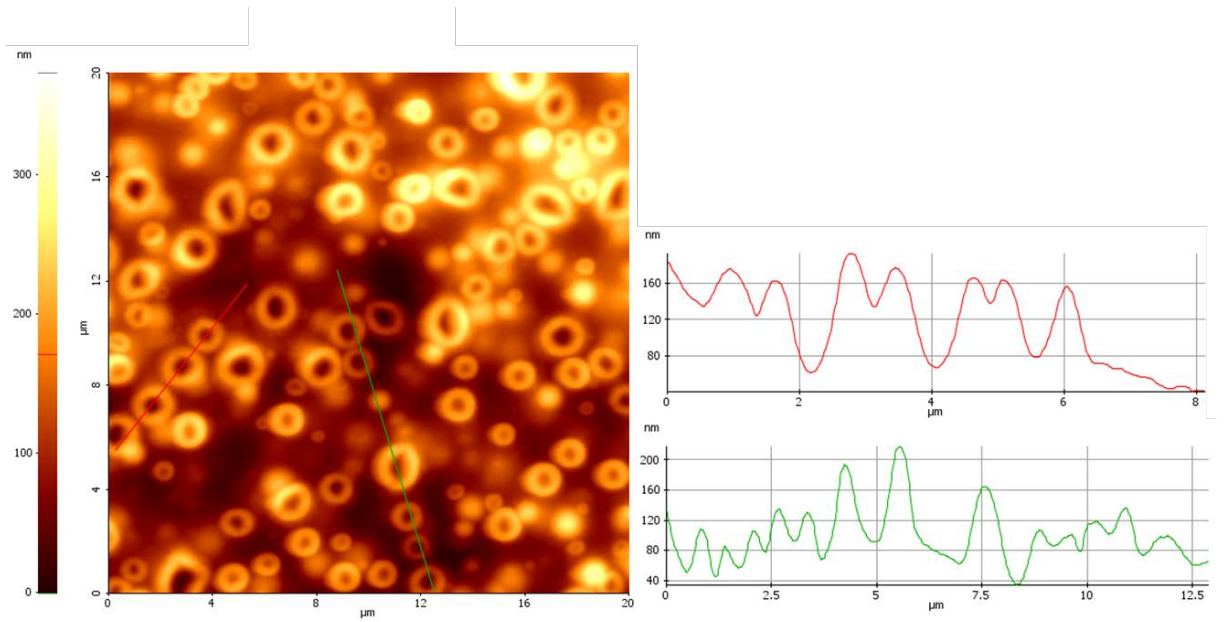
1001

1002 **Figure S15a** shows the BSA-Ch blend film RMS roughness as a function of spin speed
 1003 for all samples. RMS of polymer blends can affect coating properties such as
 1004 hydrophobicity[23] and wettability[91] and bacterial adhesion.[31] Therefore, tailorable RMS
 1005 is desirable. In all blends, roughness decreased with increased spin speed. Slopes of the 4:1
 1006 BSA-Ch blend were similar to the 2:1 blend, showing the sharpest reduction in RMS roughness
 1007 from 500 rpm to 2000 rpm. For the 4:1 blend, this is likely due to a reduction in the diameter
 1008 of all features as rpm increases. By contrast, the 2:1 blend loses large, tall features in favour
 1009 of a smooth continuous BSA domain. At 4:1, 1:1, 1:2 and 1:4 ratios, protuberances become

1010 oblate, pancake-like structures with increasing spin speed, thereby reducing RMS roughness.
1011 This also occurs in the 2:1 BSA blend, but to a lesser degree. Transitions in spin speed from
1012 500 rpm to 1000 rpm reduced protuberance height from 4 μm to 600 nm resulting in the largest
1013 decrease in RMS roughness (242 nm, **Figure S15a**). However, a smooth continuous domain
1014 appears to be the predominant feature when determining RMS roughness for this blend.

1015 **Figure S15b** plots surface area ratio (%) as a function of rotational speed in spin coating.
1016 In general, surface area ratio (%) is reduced with increased spin speed due to the reduced height
1017 of the structures. This result shows that aspect ratio of features can be tuned, allowing broader
1018 applicability. Higher aspect ratios are particularly useful for enhancing anti-reflective
1019 properties. This aligns with previous data seen with RMS roughness in **Figure S15a**. The 1:2
1020 blend deviates from the general observation by increasing surface area ratio (%) with spin
1021 speed. This is due to interconnects (necks) forming between individual protuberances. As spin
1022 speed is increased from 500 rpm to 1000 rpm (**Figure 1**, D1 and D2), protuberance growth is
1023 inhibited by faster spin speed (**Figure 2a**). Protuberances however appear interconnected by a
1024 wall structure, referred to as a neck (i.e. inhibited coalescence).[58] As viscosity increases (due
1025 to increased concentration of the continuous phase) coalescence is suppressed. This is to be
1026 expected as the adoption of a spheroidal shape is impeded.[40] These structures become more
1027 numerous as spin speed increases to 2000 rpm (**Figure 1**, D3) and growth is further inhibited.
1028 These interconnects increase the surface area ratio (%) of the sample. This is further supported
1029 by interconnects becoming less prominent at speeds exceeding 2000 rpm, though not totally
1030 removed (**Figure 1**, D4 and D5). In contrast to 4:1, 2:1 and 1:1 blends, the 1:2 blend features
1031 are compacted together and are not as well resolved from one another.

1032



1033

1034

1035

1036

Figure S16: AFM images and surface profiles of 1:4 BSA-Ch blends, 500 rpm on planar silicon substrates. Sample was etched using buffered solutions contained 200 mM Tris-HCl, pH 8.8 for 20 hrs after crosslinking with 20 wt% glutaraldehyde for 20 hr.

1037

1038

1039

1040

1041

1042

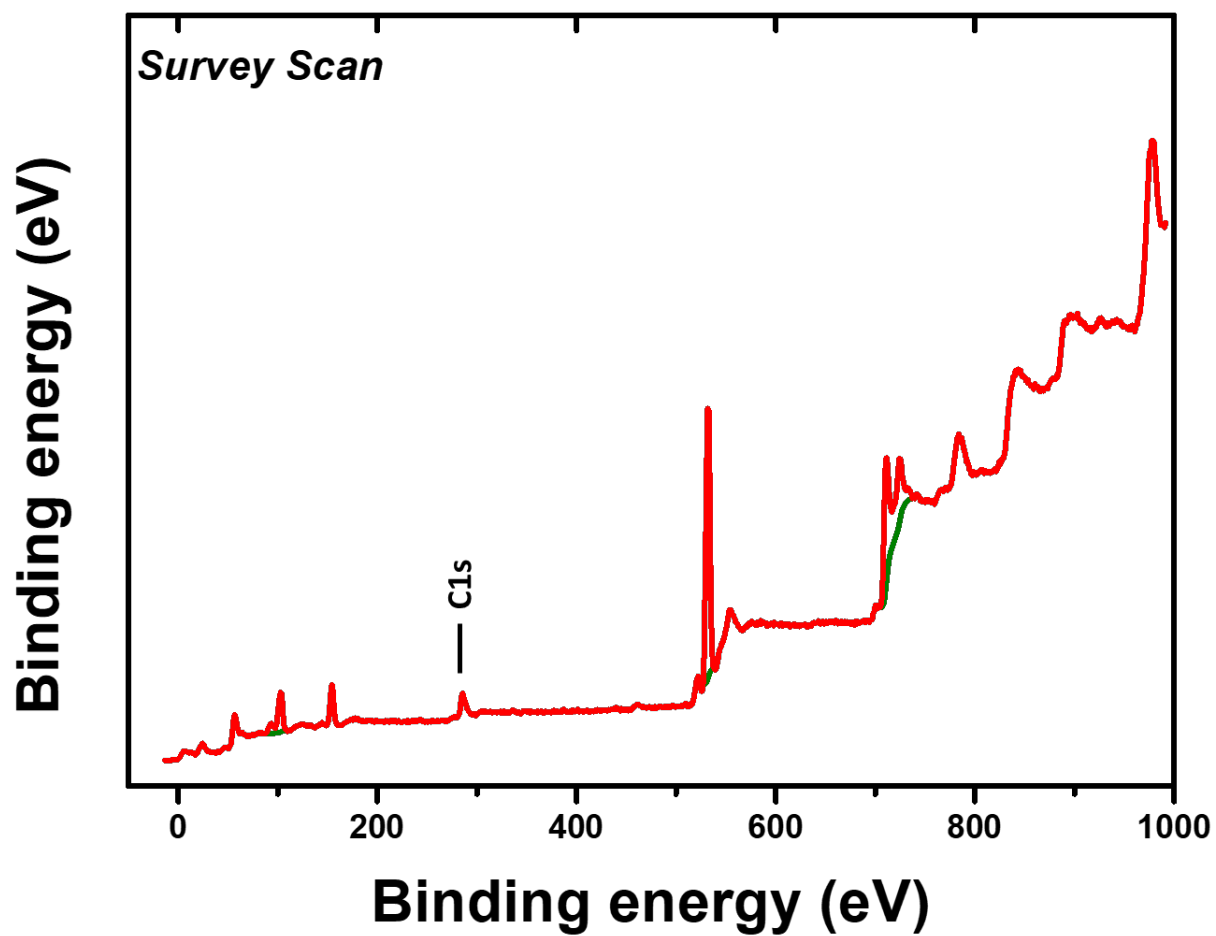
1043

1044

1045

1046

1047



1048

1049 *Figure S17: Survey spectra of porous iron oxide matrix following calcination treatment.*

1050

1051

1052

1053

1054

1055

1056

1057

1058 Pore Growth in Blend Thin-Films

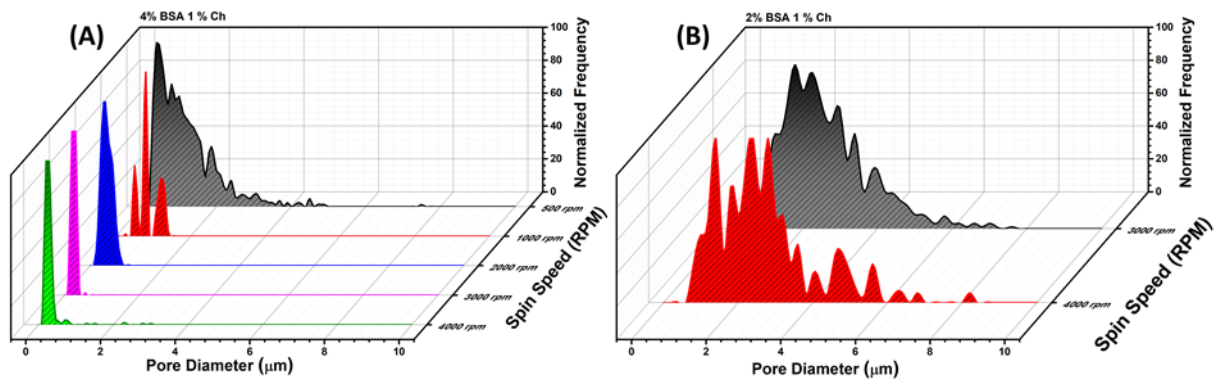
1059 At biopolymer ratio of 4 w/v% BSA to 1 w/v% Ch, across all spin speeds (**Figure 1**,
1060 Column A and **Figure S2**), pores (spherical holes) formed. Two relationships between pores
1061 and spin speed were observed: as spin speed increased, the mean pore diameter (**Figure 2a**)
1062 decreased and the number of pores per unit area (pores / μm^2 , **Figure 2b**) increased. The mean
1063 pore diameter dropped from 1.14 μm (500 rpm) to 0.25 μm (4000 rpm), **Figure 2a**. Thus, pore
1064 formation at this biopolymer ratio occurs via an inhibited growth mechanism, *i.e.* a decrease in
1065 pore diameter with faster solvent removal.[23], [34], [40] The mechanisms of pore formation
1066 vary for each blend, unlike protuberances which show a consistent formation mechanism. The
1067 2:1 BSA-Ch blend only forms “pseudo pores” (discontinuous indented regions caused by
1068 dewetting and phase inversion) at spin speeds ≥ 3000 rpm, unlike in the 4:1 blend. [15], [18],
1069 [19], [34], [92], [93] An increase in spin speed increased pore diameter and decreased the
1070 numbers of pores per area (**Figure 1**, Column B and **Figure S3**). This is in contrast to the trend
1071 observed with the 4:1 BSA-Ch blend which showed a decrease in pore diameter and an increase
1072 in pores per area with increased spin speed (**Figure 1**, Column A) which suggests a secondary
1073 phase inversion rather than salami structure formation.[17], [94]

1074 Irregularly shaped pseudo pores are generated at ≥ 3000 rpm as phase inversion occurs
1075 (**Figure 1**, B3) due to the BSA component forming a continuous phase. Differences between
1076 the protein and polysaccharide phase viscosities at the 2:1 blend ratio, and strong shear forces
1077 at high spin speeds are the cause of phase inversion and phase elongation.[18][92] These shear
1078 stress effects also contribute to the increased pore diameter, the decreased number of
1079 features/area, and the irregular pore shapes.[18], [34] The pseudo pores observed in the 2:1
1080 BSA-Ch blend are much larger than that of the pores caused by solvent-rich phase evaporation
1081 in the 4:1 blend (**Figure 1** Column A and B, **Figure 2A**). This is due to pseudo pores arising
1082 during the BSA continuous phase formation and shear effects in the 2:1 blend, whereas “true”

1083 pores in the 4:1 blend appear to be formed from a solvent rich phase and solvent evaporation
1084 upon film vitrification.[53]

1085 **Figure 1**, image B5 shows that 4000 rpm yields small, circular pores. The larger pores
1086 form longer continuous phases resulting in a minor increase of mean pore diameter. This
1087 indicates that the 2:1 BSA-Ch blend pore growth mechanism differs to that of the 4:1 blend,
1088 resulting from the formation of a continuous BSA phase.

1089 Pore diameter data was also extracted from AFM images and the corresponding
1090 normalized frequency histograms are shown in **Figure S18**. The 4:1 BSA-Ch blend pores
1091 exhibited similar growth patterns to protuberances. At low spin speeds, the blends exhibit
1092 multimodal SDs over a broad diameter range. Increasing spin speed reduces the number of
1093 modes and population weight shifts to a smaller diameter (**Figure S18a**). This suggests that the
1094 pores, like the protuberances, develop via nucleation and growth. The 2:1 BSA-Ch blend
1095 produces a multimodal pore SD at high spin speeds (**Figure S18b**). These pores are irregularly
1096 shaped and do not form via the same process as 4:1 BSA-Ch blend pores (**Figure 1**, Column
1097 A).[26] They are caused by the BSA phase inverting and forming a continuous domain.[15]
1098 As such, increasing spin speed to 4000 rpm does little to shift the pore diameter, though the
1099 blend exhibits more pronounced peaks at 1.4 μm , 1.8 μm , 2.4 μm and 2.8 μm . It must be
1100 stated, however, that phase separation of polymer blends at high humidity and resulting pore
1101 formation is poorly understood.[26] Furthermore, humidity is not typically monitored,
1102 regulated or even discussed in the majority of polymer blend literature.[95] If pores are the
1103 desired morphological structure, removal of the discontinuous domain may be a more reliable
1104 manner of achieving a porous matrix.[57]



1105

1106 **Figure S18:** Statistical analysis of BSA-Ch blends for feature diameter and frequency of
 1107 feature diameters. **A)** Displays feature frequency vs diameter of observed features for the 4:1
 1108 blends and **B)** displays feature frequency vs diameter of observed features for the 2:1 blends
 1109 respectively.

1110

1111

1112

1113

1114

1115

1116

1117

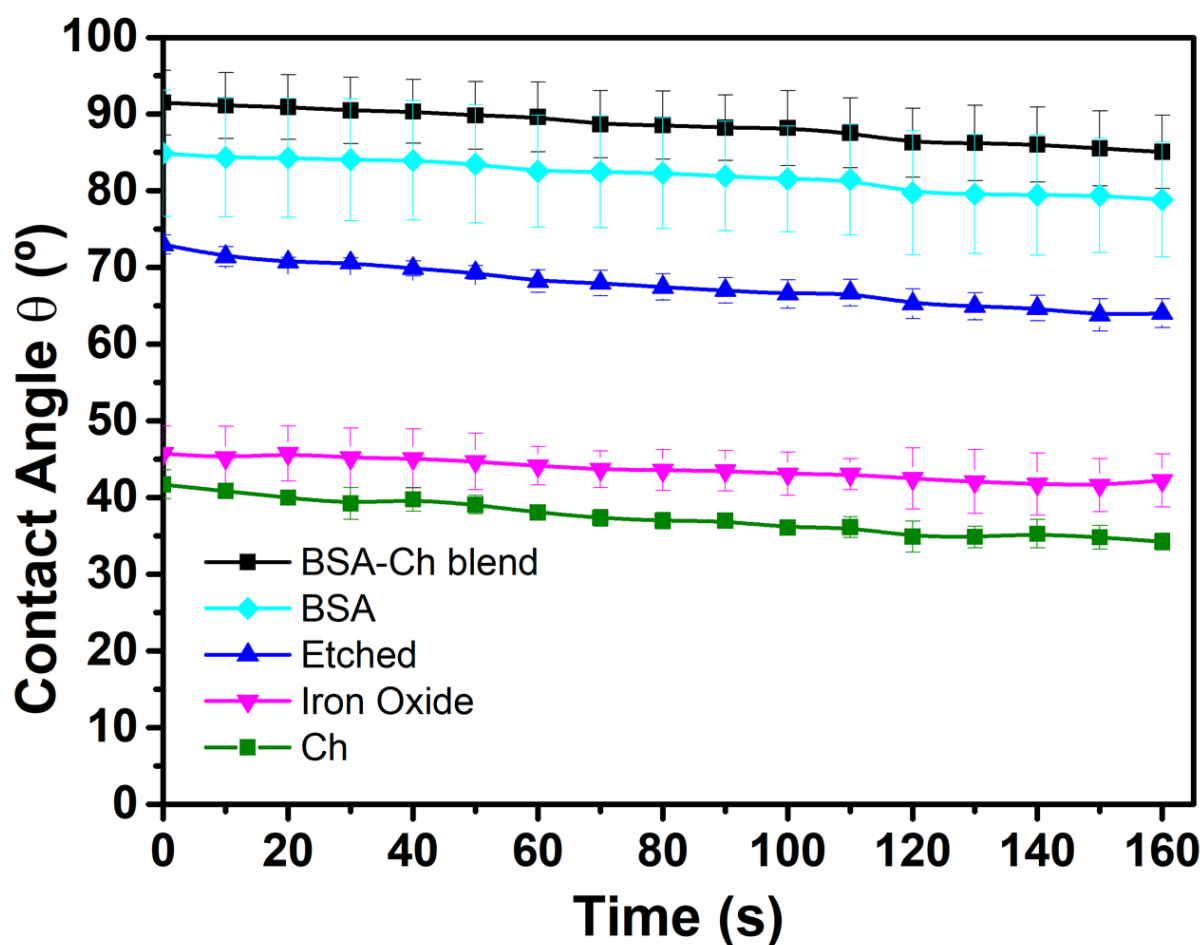
1118

1119

1120

1121

1122



1124

1125 *Figure S19: Displays plot of average receding contact angle as a function of time for*
 1126 *BSA, Ch, BSA-Ch blend, Tris-HCl etched blend and porous iron oxide matrix.*

1127 *Figure S19* shows water contact angles of the various relevant surfaces to confirm
 1128 chemical and morphological changes in the samples with processing. This is to done to confirm
 1129 the removal of BSA and the formation of a metal oxide on the surface to demonstrate correct
 1130 assignment of each domain. All tested surfaces displayed a reduction in measured contact
 1131 angle after 160 s. The 1:1 BSA-Ch blend exhibited the largest water contact angle, starting at
 1132 92° receding to 85°. This is unsurprising due to the rough nature of the blend surface and the
 1133 incorporation of BSA, which is shown to have the second largest contact angle (85° – 79°).[13]
 1134 While on its own, water contact angle measurements do not confirm the removal of BSA or

1135 formation of the metal oxide, these results compliment the findings of the etching, metal
1136 incorporation, FTIR and XPS.

1137 The porous Ch matrix ($73^\circ - 64^\circ$) has a higher contact angle than the pristine Ch surface
1138 ($42^\circ - 32^\circ$): This is due to surface roughening caused by the pores. The reduction in the contact
1139 angle, compared to the 1:1 BSA–Ch, confirms the successful removal of BSA from the blend.
1140 Finally, the water contact angle of the iron oxide film ($46^\circ - 42^\circ$) indicates magnetite
1141 composition, with the increased roughness and presence of pores contributing to a slightly
1142 larger contact angle than the literature.[96] The changes in the morphology and surface
1143 chemistry are as expected, and support the data seen in the FTIR and XPS spectra (**Figure 4**).

1144

1145